# Dynamics of roll waves

## By N. J. BALMFORTH[1,2] AND S. MANDRE[2]

[1]Departments of Mathematics and Earth & Ocean Science, University of British Columbia,
Vancouver, Canada

[2]Department of Applied Mathematics, University of California, Santa Cruz, CA 95064, USA

Shallow-water equations with bottom drag and viscosity are used to study the dynamics of roll waves. First, we explore the effect of bottom topography on linear stability of turbulent flow over uneven surfaces. Low-amplitude topography is found to destabilize turbulent roll waves and lower the critical Froude number required for instability. At higher amplitude, the trend reverses and topography stabilizes roll waves. At intermediate topographic amplitude, instability can be created at much lower Froude numbers due to the development of hydraulic jumps in the equilibrium flow. Second, the nonlinear dynamics of the roll waves is explored, with numerical solutions of the shallow-water equations complementing an asymptotic theory relevant near onset. We find that trains of roll waves undergo coarsening due to waves overtaking one another and merging, lengthening the scale of the pattern. Unlike previous investigations, we find that coarsening does not always continue to its ultimate conclusion (a single roll wave with the largest spatial scale). Instead, coarsening becomes interrupted at intermediate scales, creating patterns with preferred wavelengths. We quantify the coarsening dynamics in terms of linear stability of steady roll-wave trains.

## 1. Introduction

Roll waves are large-amplitude shock-like disturbances that develop on turbulent water flows. Detailed observations were first presented by Cornish (1910), although earlier sightings of these waves have been reported and their renditions may even appear in old artistic prints (Montes 1998). Roll waves are common occurrences in man-made conduits such as aquaducts and spillways, and have been reproduced in laboratory flumes (Brock 1969). The inception of these waves signifies that variations in flow and water depth can become substantial, both of which contribute to practical difficulties for hydraulic engineers (Rouse 1938; Montes 1998). Although most often encountered in artificial water courses, roll waves have also been seen in natural flows such as ice channels (Carver, Sear & Valentine 1999), and on gravity currents in the laboratory (Alavian 1986; Cenedese *et al.* 2004), ocean (Swaters 2003) and lakes (Fer, Lemmin & Thorpe 2003). Moreover, disturbances identified as the analogues of roll waves occur in a variety of other physical settings, such as in multi-phase fluid (Woods, Hurlburt & Hanratty 2000), mudflow (Engelund & Wan 1984), granular layers (Forterre & Pouliquen 2003), and flow down collapsible tubes and elastic conduits (with applications to air and blood flow in physiology, Pedley 1980, and a model of volcanic tremor, Julian 1994).

Waves are also common occurrences in shallow, laminar fluid films flowing on street gutters and window panes on rainy days. These objects are rationalized as
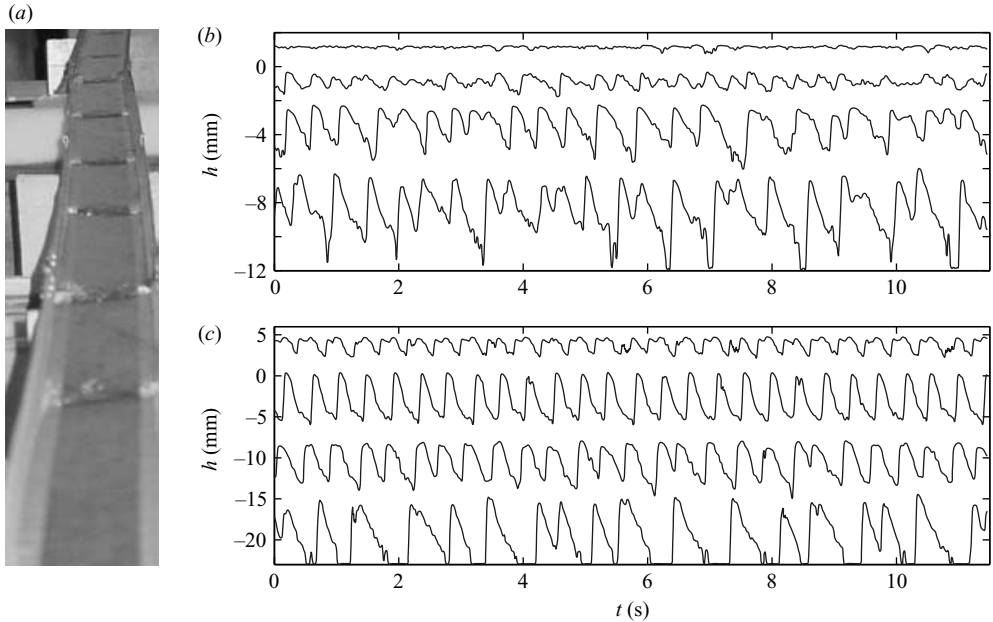
FIGURE 1. (a) A laboratory experiment in which roll waves appear on water flowing down an inclined channel. The fluid is about 1 cm deep and the channel is 10 cm wide and 18 m long; the flow speed is roughly $1 \, \mathrm{m \, s^{-1}}$. Time series of the free-surface displacements at four locations are plotted in (b) and (c). In (b), small random perturbations at the inlet seed the growth of roll waves whose profiles develop downstream (the observing stations are 3 m, 6 m, 9 m and 12 m from the inlet and the signals are not contemporaneous). (c) A similar plot for an experiment in which a periodic train was generated by moving a paddle at the inlet; as that wavetrain develops downstream, the wave profiles become less periodic and there is a suggestion of subharmonic instability.

wavy instabilities of uniform films and are the laminar relatives of the turbulent roll waves, arising typically under conditions in which surface tension plays a prominent role. As the speed and thickness of the films increases, surface tension becomes less important, and 'capillary roll waves' are transformed into 'inertial roll waves', which are relevant to some processes of mass and heat transfer in engineering. It is beyond this regime, and the transition to turbulence, that one finds Cornish's roll waves. An experiment (motivated by Brock 1969) illustrated in figure 1 shows these roll waves in the laboratory at a Reynolds number of about $10^4$ and Froude number of 3.2.

A class of models that have been used to analyse roll waves are the shallow-water equations with bottom drag and internal viscous dissipation:

$$\frac{\partial u}{\partial t} + \alpha u \frac{\partial u}{\partial x} = g \cos \phi \left( \tan \phi - \frac{\partial h}{\partial x} - \frac{\partial \zeta}{\partial x} \right) - C_f f(u, h) + \frac{1}{h} \frac{\partial}{\partial x} \left( h \nu_t \frac{\partial u}{\partial x} \right), \quad (1.1)$$

$$\frac{\partial h}{\partial t} + \frac{\partial}{\partial x} (hu) = 0, \quad (1.2)$$

where $t$ is time, $x$ is the downstream spatial coordinate, and $g$ is the gravitational acceleration. The dependent variables of this model are the depth-averaged water velocity, $u(x, t)$, and depth, $h(x, t)$; the flow configuration is illustrated in figure 2, and consists of a Cartesian coordinate system aligned with an incline of overall slope, $\tan \phi$, with $\zeta$ representing any departure due to an uneven bottom. The bottom drag
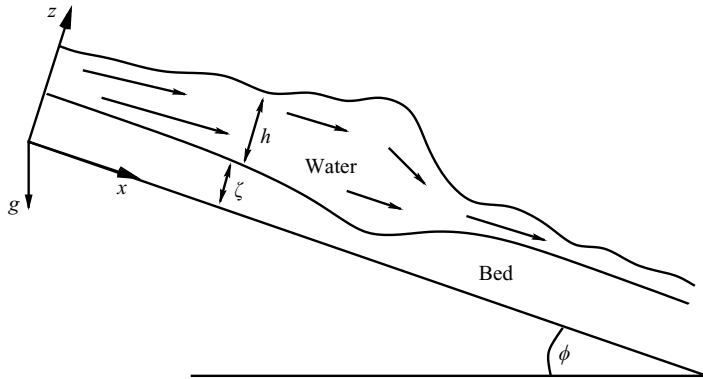
FIGURE 2. The geometry of the problem.

is $C_f f(u, h)$, where $C_f$ is a parameter, and the effective viscosity is $\nu_t$. The parameter $\alpha$ is a geometrical factor meant to characterize the flow profile in the direction transverse to the incline.

The drag law and $\alpha$ vary according to the particular model chosen, and reflect to some degree the nature of the flow. For example, the St. Venant model, popular in hydraulic engineering, pertains to turbulent stream flow. In this instance, one expects the flow profile to be fairly blunt, with sharp turbulent boundary layers, and dimensional analysis suggests a form for the drag law (a crude closure for the turbulent stress from the bed):

$$\alpha = 1, \quad f(u, h) = \frac{u|u|}{h}. \tag{1.3}$$

There are empirical estimates of the friction coefficient, $C_f$, in the drag term, which is often referred to as the Chézy formula.

For a laminar flow, the shallow-water model can be crudely justified by vertically averaging the mass and momentum balance equations, using a von Kármán–Polhausen technique to evaluate the nonlinearities (e.g. Shkadov 1967). The flow can be approximated to be parabolic in the transverse direction giving

$$\alpha = \tfrac{4}{5}, \quad f(u, h) = \frac{u}{h^2}. \tag{1.4}$$

In this instance, $C_f$ and $\nu_t$ are both given by the kinematic viscosity of the fluid. For thin films, surface tension terms must also be added to the equations; we ignore them in the present study.

In 1925, Jeffreys used the St. Venant model to provide the first theoretical discussion of roll waves. He analysed the linear stability of flow over a flat plane ($\zeta = 0$ in equation (1.1)), including the Chézy drag term and omitting the turbulent viscosity. His main result was an instability condition, $F > 2$, where $F$ is the Froude number of the flow, defined by $F = V/\sqrt{gD\cos\phi}$, where $D$ and $V$ are a characteristic fluid depth and speed. Subsequently, Dressler (1949) constructed finite-amplitude roll waves by piecing together smooth solutions separated by discontinuous shocks. The necessity of shocks in Dressler's solutions arises because, like Jeffreys, he also neglected the turbulent viscosity, which leaves the equations hyperbolic and shock forming. Needham & Merkin (1984) later added the eddy diffusion term to regularize the discontinuous shocks. Some further developments were advanced by Hwang & Chang (1987),

Prokopiou, Cheng & Chang (1991), Kranenburg (1992), Yu & Kevorkian (1992) and Chang, Demekhin & Kalaidin (2000).

Previous investigators have incorporated a variety of forms for the viscous dissipation term, all of them of the form $\nu h^{-m} \partial_x(h^n u_x)$. Of these, only those with $m = 1$ conserve momentum and dissipate energy. Furthermore, if $n = 1$, $\nu$ has the correct dimension of viscosity and the total viscous dissipation is weighted by the fluid depth. Thus we arrive at the term included in (1.1), as did Kranenburg, which we believe is the most plausible.

The study of laminar roll waves was initiated by Kapitza & Kapitza (1949) somewhat after Cornish and Jefferies. Subsequently, Benjamin (1957), Yih (1963) and Benney (1966) determined the critical Reynolds number for the onset of instability and extended the theory into the nonlinear regime. These studies exploited long-wave expansions of the governing Navier–Stokes equations to make analytical progress, and which leads to nonlinear evolution equations that work well at low Reynolds numbers. However, it was later found that the solutions of those equations diverged at higher Reynolds number (Pumir, Manneville & Pomeau 1983). This led some authors (e.g. Shkadov 1967; Alekseenko, Nakoryakov & Pokusaev 1985) to resort to the shallow-water model (1.1)–(1.2) to access such physical regimes.

The present study has two goals. First, we explore the effect of bottom topography on the inception and dynamics of roll waves ($\zeta$ is a prescribed function). Bottom topography is normally ignored in considering turbulent roll waves. However, real water courses are never completely flat, and roll waves have even been observed propagating down sequences of steps (E. Tziperman, private communication). Instabilities in laminar films flowing over wavy surfaces have recently excited interest, both theoretically (Selvarajan, Tulapurkara & Ram 1999; Cabal, Szumbarski & Floryan 2002; Floryan 2002) and experimentally (Vlachogiannis & Bontozoglou 2002), in view of the possibility that boundary roughness can promote mixing and heat and mass transfer in industrial processes, or affect the transition to turbulence. Also, in core–annular flow (a popular scenario in which to explore lubrication problems in the pipelining industry – Joseph & Renardy (1993)), there have been recent efforts to analyse the effect of periodic corrugations in the tube wall (Kouris & Tsamopoulos 2001; Wei & Runschnitzki 2002). With this background in mind, we present a study of the linear stability of turbulent flow with spatially periodic bottom topography.

Our second goal in this work is to give a relatively complete account of the nonlinear dynamics of roll waves. To this end, we solve the shallow-water equations (1.1)–(1.2) numerically, specializing to the turbulent case with (1.3), and complement that study with an asymptotic theory valid near onset. The asymptotics furnish a reduced model that encompasses as some special limits a variety of models derived previously for roll waves (Kranenburg 1992; Yu & Kevorkian 1992; Yu, Kevorkian & Haberman 2000). The nonlinear dynamics captured by the reduced model also compares well with that present in the full shallow-water system, and so offers a compact description of roll waves. We use the model to investigate the wavelength selection mechanism for roll waves. It has been reported in previous work that roll-wave trains repeatedly undergo a process of coarsening, wherein two waves approach one another and collide to form a single object, thereby lengthening the spatial scale of the wave pattern. This dynamics was documented by Brock (1969) and is also clear in the experimental data of figure 1. It has been incorrectly inferred numerically that this inverse-cascade phenomenon proceeds to a final conclusion in which only one wave remains in the domain, However, we show that coarsening does not always continue to the largest

spatial scale, but becomes interrupted and roll-wave trains emerge over a range of selected wavelengths.

We start with non-dimensionalizing our governing equations in §2. Next, in §3, we study the equilibrium flow profiles predicted by our model and follow it with a linear stability theory in §4. The asymptotic analysis is described in §5. We devote §6 to the study of the nonlinear dynamics of roll waves, mainly using the reduced model furnished by asymptotics. We summarize our results in §7. Overall, the study is focused on the turbulent version of the problem (i.e. St. Venant with (1.3)). Some of the results carry over to the laminar problem (the Shkadov model with (1.4)). However, we highlight other results which do not (see Appendix B).

A preliminary report on the current work was presented by Mandre (2001).

## 2. Mathematical formulation

We place (1.1)–(1.2) into a more submissive form by removing the dimensions from the variables and formulating some dimensionless groups. We set

$$x = L\tilde{x}, \quad u = V\tilde{u}, \quad h = D\tilde{h}, \quad \zeta = D\tilde{\zeta}, \quad t = (L/V)\tilde{t}, \qquad (2.1)$$

where

$$L = D\cot\phi, \quad C_f f(V, D) = g\sin\phi, \quad VD = Q, \qquad (2.2)$$

which specifies $D$, $L$ and $V$ in terms of the slope, friction coefficient and water flux, $Q$. We also assume that the dependence of the drag force on $u$ and $h$ is such that $f(Vu, Dh) = f(V, D)f(u, h)$. After discarding the tildes, the equations can be written in the form

$$F^2(u_t + \alpha u u_x) + h_x + \zeta_x = 1 - f(u, h) + \frac{\nu}{h}(h u_x)_x \qquad (2.3)$$

and

$$h_t + (hu)_x = 0, \qquad (2.4)$$

where the two dimensionless groups,

$$F^2 \equiv \frac{V^2}{gD\cos\phi}, \quad \nu = \frac{\nu_t V}{C_f L^2 f(V, D)}, \qquad (2.5)$$

are the square of the Froude number and a dimensionless viscosity parameter, assumed constant. As demanded by the physical statement of the problem, that the flow is shallow, we typically take $\nu$ to be small, so that the bottom drag dominates the internal viscous dissipation. In this situation, we expect that the precise form of the viscous term is not important.

We impose periodic boundary conditions in $x$. This introduces the domain length as a third dimensionless parameter of the problem. As mentioned earlier, we also select topographic profiles for $\zeta(x)$ that are periodic. For the equilibria, considered next, we fix the domain size to be the topographic wavelength, but when we consider evolving disturbances we allow the domain size to be different from that wavelength.

## 3. Equilibria

The steady flow solution, $u = U(x)$ and $h = H(x)$, to (2.3)–(2.4) satisfies

$$F^2 \alpha U U_x + H_x + \zeta_x = 1 - f(U, H) + \frac{\nu}{H}(H U_x)_x, \quad HU = 1, \qquad (3.1)$$
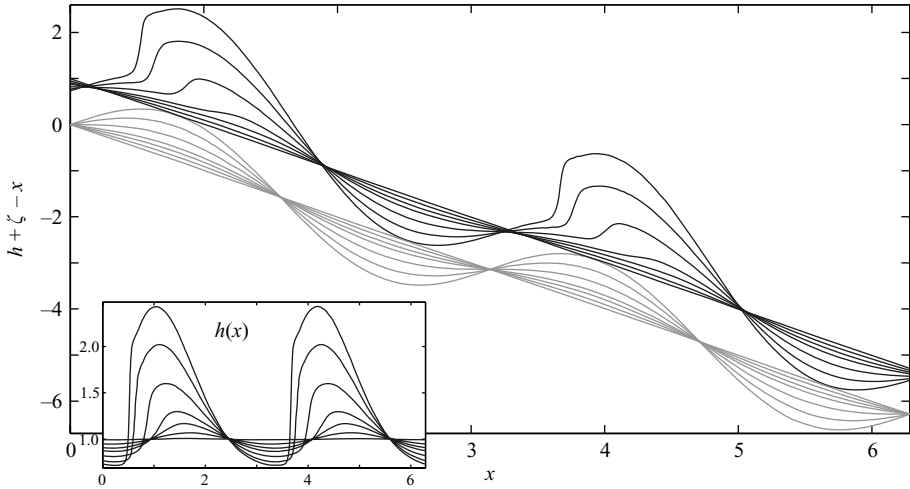
FIGURE 3. Viscous periodic equilibria for $\hat{F} = \sqrt{\alpha}F = 1.225$, $k_b = 2$ and $\nu = 0.04$, with varying $a$ (0.01, 0.1, 0.2, 0.3, 0.5, 0.75 and 1).

since we have used the water flux $Q$ to remove dimensions. For both drag laws (1.3) and (1.4), $f(U, H) = U^3$. Also, by taking $\hat{F} = F\sqrt{\alpha}$ as a modified Froude number, we avoid a separate discussion of the effect of $\alpha$.

By way of illustration, we consider a case with sinusoidal bottom topography:

$$\zeta(x) = a\cos k_b x, \tag{3.2}$$

where $k_b$ is the wavenumber of the bottom topography and $a$ is its amplitude. Discussion on more general topographic profiles is included in §7. Some example equilibria are illustrated in figure 3. For low-amplitude topography, the response in the fluid depth appears much like $\zeta$, with a phase shift. As the amplitude increases, however, steep surface features appear. A similar trend was experimentally observed by Vlachogiannis & Bontozoglou (2002) which they reported as a 'resonance'. We rationalize these features in terms of hydraulic jumps, based on the 'inviscid' version of the problem (i.e. $\nu = 0$).

For $\nu = 0$, the equilibria equation simplifies and can be written in the form

$$H_\eta = \left[\frac{H^3(1 - f(1/H, H) - k_b\zeta_\eta)}{k_b(H^3 - \hat{F}^2)}\right] \tag{3.3}$$

where $\eta = k_b x$. All solutions to (3.3) reside on the $(\eta, H)$ phase plane; we require only those that are strictly periodic in $\eta$. Now, the extrema of $H(\eta)$ occur for $H = 1/(1 - k_b\zeta_\eta)^{1/3}$, whilst there is a singular point at $H = \hat{F}^{2/3}$. In general, $H(\eta)$ becomes vertical at the latter point, except if the numerator also vanishes there, in which case inviscid solutions may then pass through with finite gradient. Overall, the two curves, $H = 1/(1 - k_b\zeta_\eta)^{1/3}$ and $H = \hat{F}^{2/3}$, organize the geometry of the inviscid solutions on the $(\eta, H)$ phase plane. Four possible geometries emerge, and are illustrated in figure 4.

The two curves cross when $\hat{F}^2 = 1/(1 - k_b\zeta_\eta)$ somewhere on the $(\eta, H)$-plane. Thus, if the amplitude of the topography is defined so that $-a \leqslant \zeta'(\eta) \leqslant a$, the curves cross when

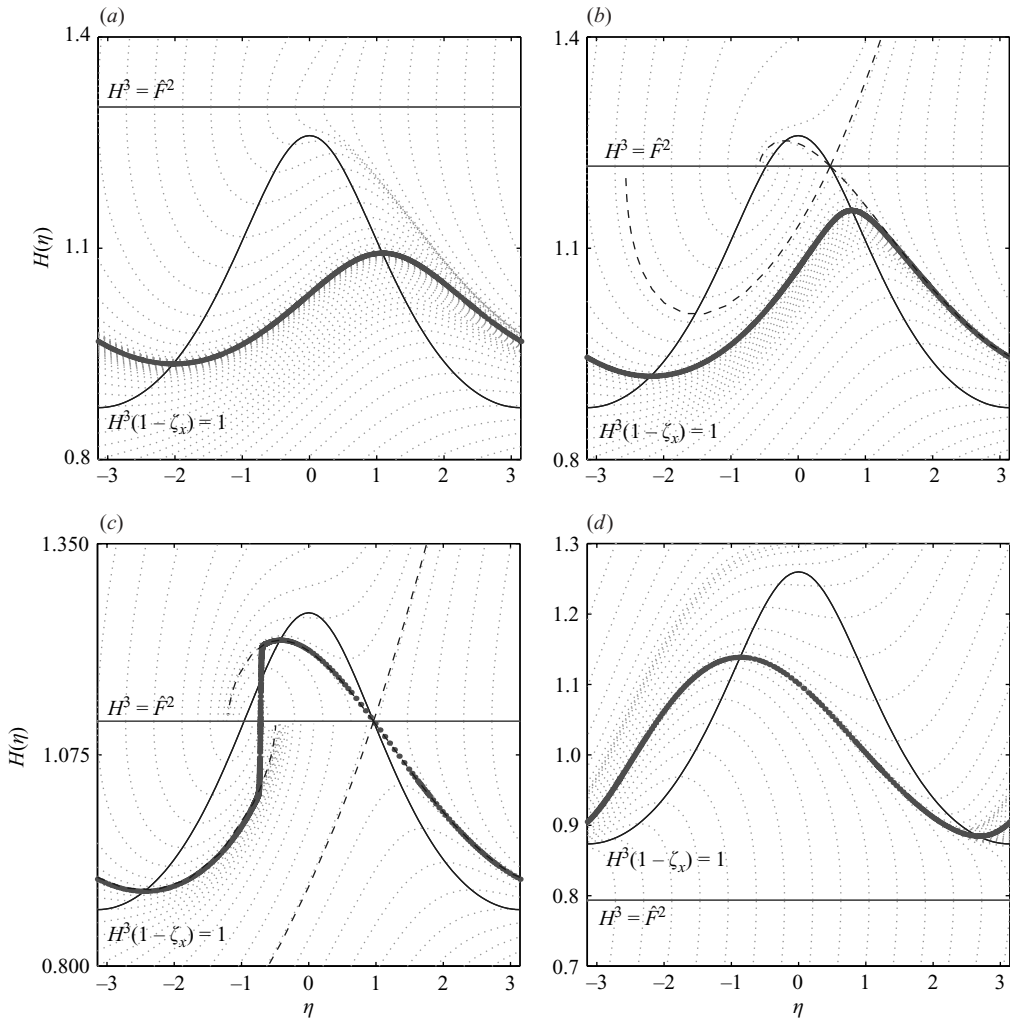$$(1 + k_b a)^{-1/2} < \hat{F} < (1 - k_b a)^{-1/2} \tag{3.4}$$

FIGURE 4. Stationary flow profiles for $k_b = 5$, $a = 0.1$ and four values of $\hat{F} = F\sqrt{\alpha}$: (a) 2.2, (b) 1.8, (c) 1.4, (d) 0.5. Light dotted curves show a variety of inviscid solutions ($\nu = 0$) to illustrate the flow on the phase plane ($\eta$, $H$). The curve of thicker dots shows a periodic viscous solution (with $\nu = 0.002$). Also included is the line $H = \hat{F}^{2/3}$ and the curve $H = (1 - \zeta_x)^{-1}$. In (b) and (c), with dashed lines, we further show the inviscid orbits that intersect the 'crossing point', $H = \hat{F}^{2/3} = (1 - \zeta_x)^{-1}$.

(if $k_b a > 1$, there is no upper bound on $\hat{F}$). Outside this range, the inviscid system has smooth periodic solutions, and figures 4(a) and 4(d) illustrate the two possible cases.

When $\hat{F}$ falls into the range in (3.4), the two organizing curves cross, and the geometry of the phase plane becomes more complicated. For values of $\hat{F}$ adjacent to the two limiting values in (3.4), periodic inviscid solutions still persist and lie either entirely above or below $H = \hat{F}^{2/3}$ (figure 4b). We denote the ranges of Froude number over which the solutions persist by $(1 + k_b a)^{-1/2} < \hat{F} < F_1$ and $F_2 < \hat{F} < (1 - k_b a)^{-1/2}$. At the borders, $F_1$ and $F_2$, the inviscid periodic solutions terminate by colliding with a crossing point. Thereafter, in $F_1 < \hat{F} < F_2$, no periodic, continuous solution exists:
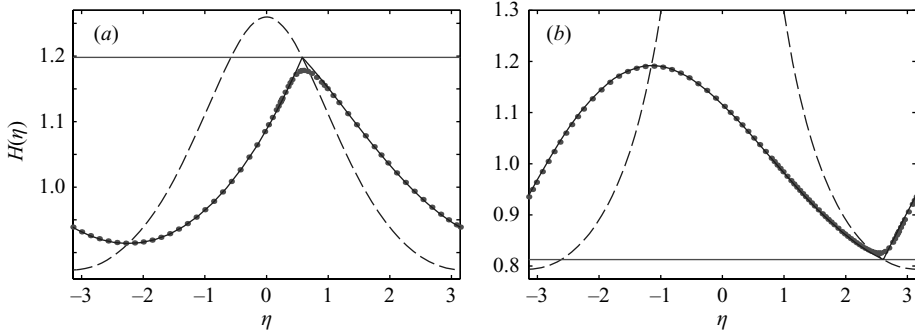
FIGURE 5. Limiting periodic inviscid solutions for $a = 0.1$, and (a) $k_b = 5$ and $\hat{F} \approx 1.311$, (b) $k_b = 10$ and $\hat{F} \approx 0.733$. The dots (which lies underneath the inviscid solution except near the corner at the rightmost crossing point) show the viscous counterparts for $\nu = 0.002$.

all trajectories on the phase plane either diverge to $H \to \infty$ or become singular at $H = \hat{F}^{2/3}$ (figure 4c).

Although there are no periodic inviscid solutions within the divergent range of Froude numbers, $F_1 < \hat{F} < F_2$, there are periodic, weakly viscous solutions that trace out inviscid trajectories for much of the period (see figure 4). The failure of the inviscid trajectories to connect is resolved by the weakly viscous solution passing through a hydraulic jump over a narrow viscous layer. The limiting inviscid jump conditions can be determined by integrating the conservative form of the governing equations across the discontinuity:

$$U_+ H_+ = U_- H_- = 1, \quad \hat{F}^2 U_+ + \frac{H_+^2}{2} = \hat{F}^2 U_- + \frac{H_-^2}{2}, \tag{3.5}$$

where the subscripts $+$ and $-$ denote the values downstream and upstream respectively.

The jump region, $F_1 < \hat{F} < F_2$, is delimited by values of the Froude number at which an inviscid solution curve connects the rightmost crossing point to itself modulo one period. This curve is continuous, but contains a corner at the crossing point; see figure 5. The curves $F_1$ and $F_2$ are displayed on the $(\hat{F}, k_b a)$-plane in figure 6. Hydraulic jumps form in the weakly viscous solutions in the region between these curves.

A departure from the classification shown in figure 4 occurs for Froude numbers near unity and low-amplitude topography. Here, the flow of the inviscid solutions on the $(\eta, H)$-phase plane is sufficiently gently inclined to allow orbits to pass through both crossing points. This leads to a fifth type of equilibrium, as shown in figure 7. Although this solution is continuous, its gradient is not; again, there is a weakly viscous counterpart. As the amplitude of the topography increases, the flow on the phase plane steepens, and eventually the inviscid orbit disappears (see figure 7), to leave only viscous solutions with hydraulic jumps. This leads to another threshold, $\hat{F} = F_*$, on the $(\hat{F}, k_b a)$-plane, which connects the $F_1$ and $F_2$ curves across the region surrounding $\hat{F} = 1$ (see the inset of figure 6).

## 4. Linear stability theory

We perform a linear stability analysis of the steady states described above to uncover how the bed structure affects the critical Froude number for the onset of roll
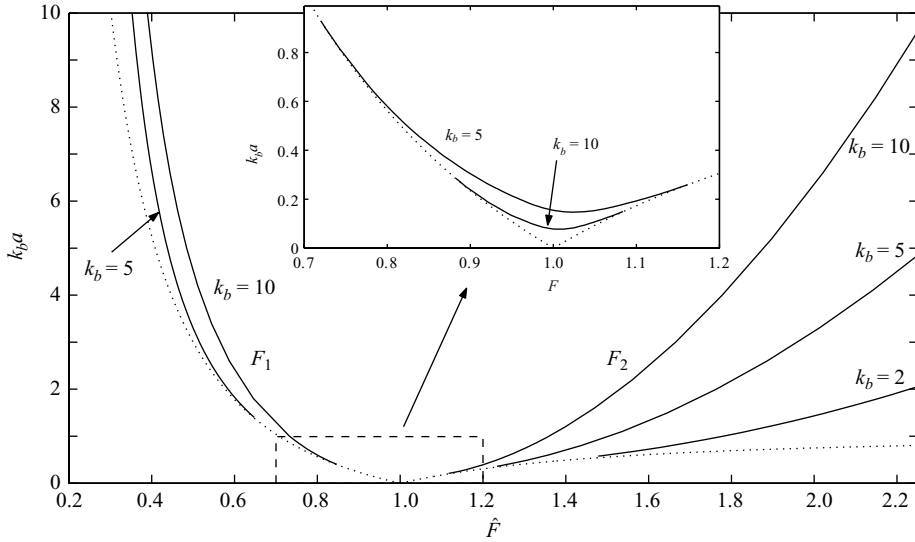
FIGURE 6. The jump region on the $(\hat{F}, k_b a)$-plane. The solid lines show the limits, $F_1$ and $F_2$, for $k_b = 5$ and 10; the $F_2$ curve is also shown for $k_b = 2$. Shown by dotted lines are the borders (3.4) of the region in which the organizing curves $H = \hat{F}^{2/3}$ and $H = (1 - \zeta_x)^{-1/3}$ cross one another. The inset shows a magnification near $\hat{F} = 1$, and the curves $F = F_*(a)$ on which the inviscid solutions passing through both crossing points disappear.
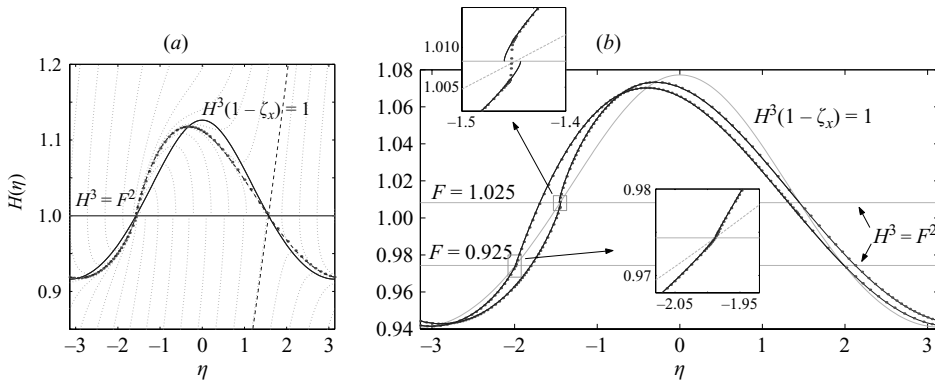


FIGURE 7. (a) Stationary flow profile for $k_b = 3$, $a = 0.1$ and $\hat{F} = 1$; the various curves have the same meaning as in figure 4. (b) Breakage of the inviscid curve passing through both crossing points for $k_b = 5$ and $a = 0.4$. Two equilibria are shown, with $\hat{F} = 0.925$ and 1.025. Dots show weakly viscous solutions with $\nu = 2 \times 10^{-3}$.

waves. Let $u = U(x) + u'(x, t)$ and $h = H(x) + h'(x, t)$. After substituting these forms into the governing equations and linearizing in the perturbation amplitudes, we find the linear equations,

$$F^2[u_t' + \alpha(Uu')_x] + h_x' = -f_h h' - f_u u' + \nu u_{xx}' \qquad (4.1)$$

$$h_t' + (Uh' + Hu')_x = 0, \qquad (4.2)$$

where $f_u = (\partial f / \partial u)_{u=U,h=H}$ and $f_h = (\partial f / \partial h)_{u=U,h=H}$ denote the partial derivatives of the drag law, evaluated with the equilibrium solution.

Because of the spatial periodicity of the background state, a conventional stability analysis must proceed by way of Floquet, or Bloch, theory. We represent infinitesimal perturbations about the equilibria by a truncated Fourier series with a Bloch wavenumber, $K$ (a Floquet multiplier), and growth rate, $\sigma$:

$$u' = \sum_{j=-N+1}^{N} u_j e^{ijk_b x + iKx + \sigma t}, \quad h' = \sum_{j=-N+1}^{N} h_j e^{ijk_b x + iKx + \sigma t}. \tag{4.3}$$

We introduce these solutions into the governing equations and then linearize in the perturbation amplitudes, to find an algebraic eigenvalue equation for $\sigma$. The system contains five parameters: the Froude number ($F$), wavenumber of bottom topography ($k_b$), amplitude of bottom topography ($a$), the Bloch wavenumber ($K$) and the diffusivity ($\nu$).

When the bottom is flat, the equilibrium is given by $U = H = 1$ and we avoid the Bloch decomposition by taking $(u', h') \propto \exp(ikx)$. This leads to the dispersion relation,

$$\sigma = -ik \frac{1+\alpha}{2} - \frac{f_u + \nu k^2}{2} \pm \sqrt{\left[ \frac{f_u + \nu k^2}{2F^2} + \frac{(\alpha - 1)ik}{2} \right]^2 + \frac{ik f_h - k^2}{F^2}}. \tag{4.4}$$

For long waves, the least stable root becomes

$$\sigma \sim -ik \left[ \frac{f_u}{f_h} - 1 \right] + \left[ \frac{F^2 \left( f_u f_h (\alpha - 1) + f_h^2 \right) - f_u^2}{f_u^3} \right] k^2 + \cdots \tag{4.5}$$

which displays the instability condition,

$$F^2 > \frac{f_u^2}{f_u f_h (\alpha - 1) + f_h^2}. \tag{4.6}$$

For the turbulent case, $f_u = 2$ and $f_h = -1$, and so $F > 2$, as found by Jeffreys. For the laminar case, on the other hand, $f_u = 1$ and $f_h = -2$, which gives $F > \sqrt{5/22}$.

We next provide a variety of numerical solutions to the linear stability problem for finite topography with the sinusoidal profile, $\zeta = a \sin(k_b x)$, and using the St. Venant model ($f = u^2/h$ and $\alpha = 1$). In this instance, the Bloch wavenumber allows us to analyse the stability of wavenumbers which are not harmonics of $k_b$. We only need to consider

$$-\frac{k_b}{2} < K \leqslant \frac{k_b}{2}; \tag{4.7}$$

values of $K$ outside this range do not give any additional information because the wavenumber combination, $k = jk_b + K$ for $j = 0, 1, 2, \ldots$, samples the full range.

The dependence of the growth rate on $k$ is illustrated in figure 8 for three Froude numbers straddling $F = 2$ and a low-amplitude topography. The case with larger Froude number is unstable to a band of waves with small wavenumber, and illustrates how the instability invariably has a long-wave character. This feature allows us to locate the boundaries of neutral stability by simply taking $K$ to be small (as done below).

A key detail of this stability problem is that low-amplitude topography is *destabilizing*. We observe this feature in figure 9, which shows the curve of neutral stability on the $(F, a)$-plane for fixed Bloch wavenumber, $K = 10^{-3}$, and three values of $\nu$, including $\nu = 0$. The curves bend to smaller $F$ on increasing $a$, indicating how the unstable region moves to smaller Froude number on introducing topography.
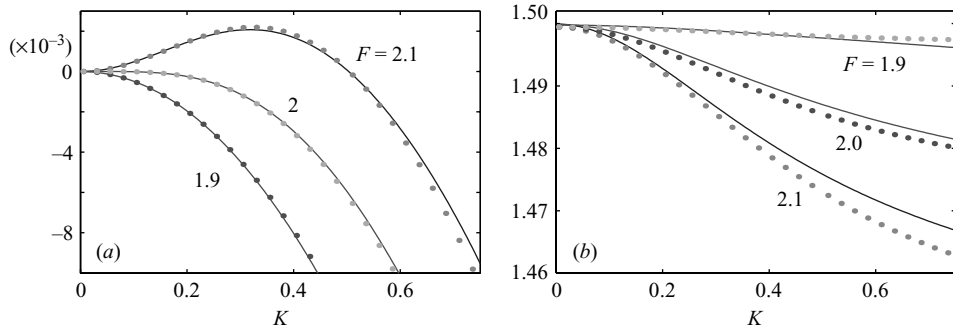
FIGURE 8. Eigenvalues from numerical stability analysis and asymptotics for $\nu = 0.4$, $k_b = 10$, $a = 0.05$, and Froude numbers of 1.9, 2 and 2.1. The lines denote numerical calculations and the dots represents asymptotic theory (for $\nu \sim k_b^{-1}$; theory A). (a) The growth rate, $\text{Re}(\sigma)$, and (b) the phase speed, $-\text{Im}(\sigma)/K$.
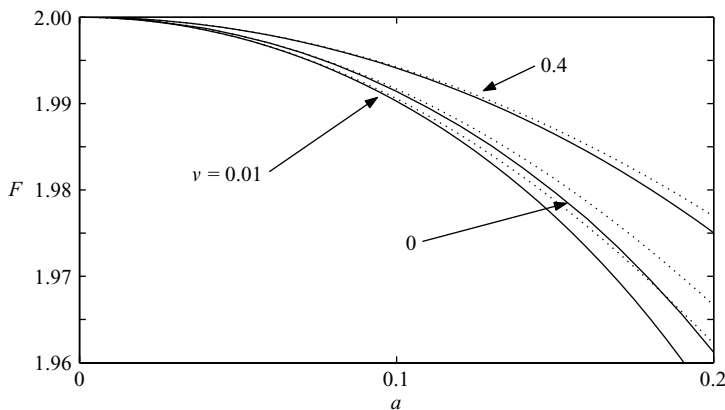


FIGURE 9. Stability boundaries on the $(a, F)$-plane, near $(a, F) = (0, 2)$, for fixed Bloch wavenumber, $K = 10^{-3}$, and three values of viscosity (0, 0.01 and 0.1). Also shown are the boundaries predicted by the two versions of asymptotic theory (theory A is used for $\nu = 0.1$, and theory B for $\nu = 0.01$ and 0).

In this region of parameter space, we find that viscosity plays a dual role: as is clear from the classical result for a flat bottom, viscosity stabilizes roll waves of higher wavenumber; in conjunction with topography, however, viscosity can destabilize long waves, see figures 9 and 10. The second figure shows the depression of the $F = 2$ stability boundary on the $(\nu, F)$-plane as the bottom topography is introduced. The boundary rebounds on increasing the viscosity further, and so the system is most unstable for an intermediate value of the viscosity (about 0.1 in the figures). These results expose some dependence on $\nu$, which presumably also reflects the actual form of the viscous term. Nevertheless, the 'inviscid', $\nu \to 0$, results can also be read off the figures and are independent of that form. It is clear from figures 9 and 10 that the general trend is to destabilize turbulent roll waves.

Further from $(a, F) = (0, 2)$, a new form of instability appears that extends down to much smaller Froude number, see figure 11($a$). The growth rate increases dramatically in these unstable windows, as shown further in figure 11($b$). In fact, for $\nu = 0$, it appears
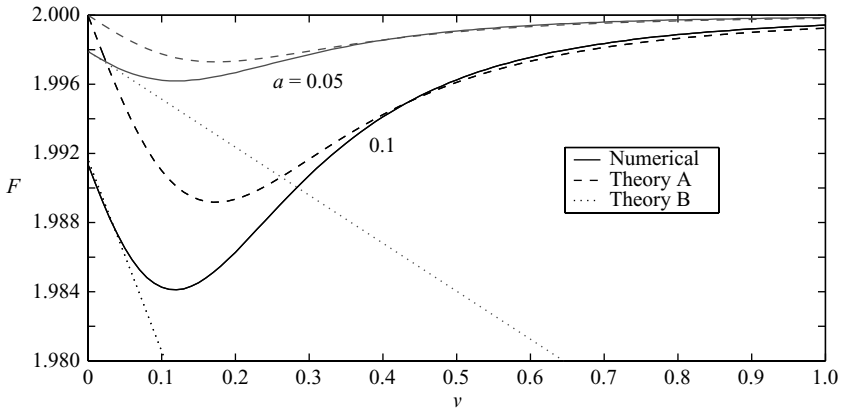
FIGURE 10. Stabilities boundaries on the $(v, F)$-plane, near $a = 0$, for fixed Bloch wavenumber, $K = 10^{-3}$, and $k_b = 10$. Also shown are the boundaries predicted by the two versions of asymptotic theory (labelled A and B).
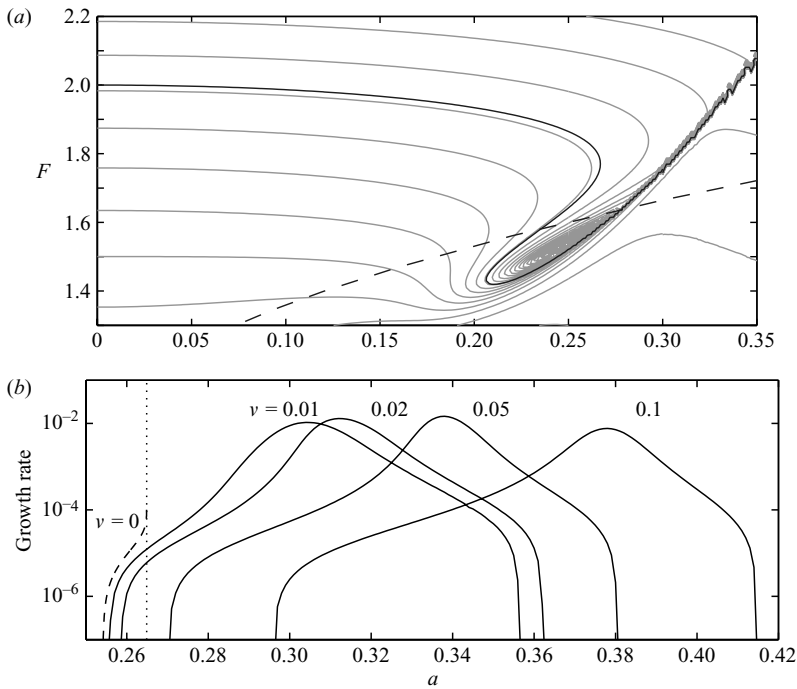


FIGURE 11. Instability windows at smaller Froude number. (*a*) Contours of constant growth rate ($\sigma$) for $v = 0.05$, $k_b = 10$, $K = 10^{-3}$. Thirty equally spaced contours (lighter lines) are plotted with the growth rate going from $1.14 \times 10^{-4}$ to $-4.28 \times 10^{-5}$. The darker line denotes the neutral stability curve and the dashed line shows the location of the $F_2$-curve. (*b*) Growth rates against $a$ for $F = 1.6$, $k_b = 5$, $K = 10^{-3}$ and four values of $v$. These sections cut through the window of instability at smaller Froude number. Also shown is the inviscid growth rate, which terminates as $F \rightarrow F_2$ (the vertical dotted line).

as though the growth rate as a function of $a$ becomes vertical, if not divergent (we have been unable to resolve precisely how the growth rate behaves, although a logarithmic dependence seems plausible). This singular behaviour coincides with the approach of
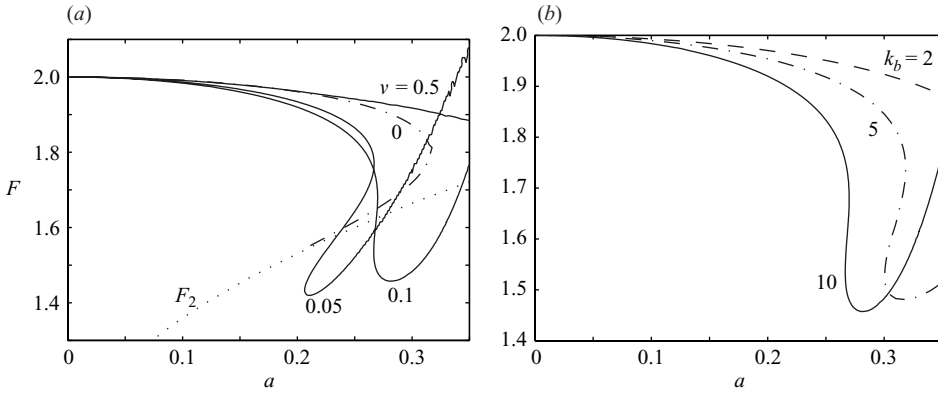
FIGURE 12. Stability boundaries for (*a*) different viscosities, with $k_b = 10$ and $K = 10^{-3}$ and (*b*) different wavenumbers of bottom topography ($k_b$), with $\nu = 0.1$ and $K = 10^{-3}$.

the inviscid equilibrium to the limiting solution with $F = F_2$. In other words, when the equilibrium forms a hydraulic jump, the growth rate of linear theory becomes singular (in gradient, and possibly even in value). The weakly viscous solutions show no such singular behaviour, the jump being smoothed by viscosity, but the sharp peak in the growth rate remains, and shifts to larger $a$ (figure 11). As a result, the unstable windows fall close to the $F_2$-curve of a neighbouring inviscid equilibrium; a selection of stability boundaries displaying this effect are illustrated in figure 12. However, we have not found any comparable destabilization near the $F_1$-curve. In fact, near the $F_1$-curve, the growth rates appear to decrease, suggesting that the hydraulic jump in this part of the parameter space is stabilizing.

Figure 12 also brings out another feature of the stability problem: for larger $a$, the stability boundaries curve around and pass above $F = 2$. Thus, large-amplitude topography is stabilizing.

### 4.1. *An integral identity for inviscid flow*

When $\nu = 0$, an informative integral relation can be derived from the linear equations by multiplying (4.1) by $2h'U - Hu'$ and (4.2) by $2F^2Uu' - h'$, then integrating over $x$ and adding the results:

$$\frac{\mathrm{d}}{\mathrm{d}t} \left\langle F^2 H \left( u' - \frac{h'U^2}{2} \right)^2 + h'^2 \left( 1 - \frac{F^2U^2}{4H} \right) \right\rangle$$

$$= -\langle U(2u' - U^2h')^2 \rangle - \left\langle 3U_x \left( F^2u'^2 H + \frac{h'^2}{4} \right) \right\rangle, \quad (4.8)$$

where the angular brackets denote $x$-integrals.

For the flat bottom, $U = H = 1$, and the left-hand side of this relation is the time derivative of a positive-definite integral provided $F < 2$. The right-hand side, on the other hand, is negative definite. Thus, for such Froude numbers, the integral on the left must decay to zero. In other words, the system is linearly stable, and so (4.8) offers a short-cut to Jeffrey's classical result.

Because of the integral involving $U_x$, a stability result is not so straightforward with topography, although (4.8) still proves useful. First, assume that this new integral is overwhelmed by the first term on the right of (4.8), so that the pair remain negative definite. This will be true for low-amplitude topography, away from the

region in which hydraulic jumps form. Then stability is assured if $1 > F^2 U^2/(4H)$ or $F < 2\sqrt{H}/U$. That is, if the *local* Froude number is everywhere less than 2 (a natural generalization of Jeffrey's condition).

Second, consider the case when the local Froude number condition is everywhere satisfied, so that stability is assured if the right-hand side of (4.8) is always negative. But on raising the amplitude of the topography, $U_x$ increases sharply as a hydraulic jump develops in the equilibrium flow. Provided $U_x < 0$ at that jump, the right-hand side of (4.8) can then no longer remain always negative, and allowing an instability to become possible. As illustrated in figure 4, the jump in $H$ is positive across the $F_2$-curve, so $U_x < 0$, and that feature is potentially destabilizing, as indicated in the stability analysis. Nonetheless, we have found no explanation for why the jump near $F_2$ is destabilizing but the one near $F_1$ is not.

## 5. Asymptotics

We complement the linear stability analysis with an analytical theory based on asymptotic expansion with multiple time and length scales. The theory is relevant near onset for low-amplitude but rapidly varying topography, and proceeds in a similar fashion to that outlined by Yu & Kevorkian (1992) and Kevorkian, Yu & Wang (1995) for flat planes; topography is incorporated by adding a further, finer length scale. We offer two versions of the theory, suited to different asymptotic scalings of the viscosity parameter, $\nu$. We refer to the two versions as theories A and B.

### 5.1. *A first expansion; $\nu \sim \epsilon$ (theory A)*

We take $\epsilon \equiv k_b^{-1} \ll 1$ and $\zeta$ to be an $O(\epsilon)$ function of the coordinate, $\eta = x/\epsilon$, resolving the rapid topographic variation, $\zeta \to \epsilon A(\eta)$, where $A(\eta)$ describes the topographic profile. We introduce the multiple length and time scales, $(\eta, x)$ and $(t, \tau)$, where $\tau = \epsilon t$, giving

$$\partial_t \to \partial_t + \epsilon \partial_\tau, \quad \partial_x \to \frac{1}{\epsilon}\partial_\eta + \partial_x, \tag{5.1}$$

and further set

$$\nu = \epsilon \nu_1, \quad F = F_0 + \epsilon F_1. \tag{5.2}$$

We next expand the dependent variables in the sequences,

$$u = 1 + \epsilon[U_1(\eta) + u_1(x, t, \tau)] + \epsilon^2[U_2(\eta, x, t, \tau) + u_2(x, t, \tau)]$$
$$+ \epsilon^3[U_3(\eta, x, t, \tau) + u_3(x, t, \tau)] + \dots, \tag{5.3}$$
$$h = 1 + \epsilon[H_1(\eta) + h_1(x, t, \tau)] + \epsilon^2[H_2(\eta, x, t, \tau) + h_2(x, t, \tau)]$$
$$+ \epsilon^3[H_3(\eta, x, t, \tau) + h_3(x, t, \tau)] + \dots. \tag{5.4}$$

Here, $U_1$ and $H_1$ denote the fine-scale corrections due to the topography, whereas $u_1$ and $h_1$ represent the longer-scale, wave-like disturbance superposed on the equilibrium. To avoid any ambiguity in this splitting, we demand that $U_1$ and $H_1$ have zero spatial average. At higher order, we again make a separation into fine-scale and wave components, but the growing disturbance modifies the local flow on the fine scale and so, for example, $U_2$ and $H_2$ acquire an unsteady variation.

At leading order, we encounter the equations,

$$F_0^2 U_{1\eta} + H_{1\eta} + A_\eta = \nu_1 U_{1\eta\eta}, \quad U_{1\eta} + H_{1\eta} = 0, \tag{5.5}$$

and write the solution formally as

$$U_1 = f(\eta) \equiv -H_1, \tag{5.6}$$

where $f(\eta)$ has zero spatial average. A convenient way to compute $f(\eta)$ is via a Fourier series. Let

$$A(\eta) = \sum_{j=1}^{\infty} A_j e^{ij\eta} + \text{c.c.}, \tag{5.7}$$

where the coefficients $A_j$ are prescribed (without loss of generality we may take $A(\eta)$, i.e. $\zeta$, to have zero spatial average). Then,

$$f = \sum_{j=1}^{\infty} f_j e^{ij\eta} + \text{c.c.}, \quad f_j = -\frac{A_j \exp(i\theta_j)}{\sqrt{\left(F_0^2 - 1\right)^2 + \nu_1^2 j^2}}, \quad \tan\theta_j = \frac{\nu_1 j}{F_0^2 - 1}. \tag{5.8}$$

At next order:

$$F_0^2 U_{2\eta} + H_{2\eta} - \nu_1 U_{2\eta\eta} = -F_0^2(u_{1t} + u_{1x}) - h_{1x} - 2u_1 + h_1$$
$$- F_0^2 u_1 U_{1\eta} - F_0^2 U_1 U_{1\eta} - 2U_1 + H_1 - 2F_0 F_1 U_{1\eta} + \nu_1 H_{1\eta} U_{1\eta}, \quad (5.9)$$

$$U_{2\eta} + H_{2\eta} = -h_{1t} - h_{1x} - u_{1x} - (H_1 U_1)_\eta - (h_1 U_1 + H_1 u_1)_\eta. \tag{5.10}$$

We deal with these equations in two stages. First, we average over the fine length scale $\eta$ to eliminate the corrections, $U_2$ and $H_2$. This generates our first set of evolution equations for the variables $u_1$ and $h_1$:

$$F_0^2(u_{1t} + u_{1x}) + h_{1x} + 2u_1 - h_1 = -\nu_1 \overline{U_{1\eta}^2}, \tag{5.11}$$
$$h_{1t} + h_{1x} + u_{1x} = 0. \tag{5.12}$$

This pair of equations has the characteristic coordinates, $\xi = x - (1 + F^{-1})t$ and $\tilde{\xi} = x - (1 - F^{-1})t$. Moreover, along the characteristics, the solutions either grow or decay exponentially unless the undifferentiated terms in (5.11) cancel. To avoid such detrimental behaviour, we demand that those terms vanish, which fixes

$$h_1(\xi) = 2u_1(\xi) + \nu_1 \overline{U_{1\eta}^2} \tag{5.13}$$

and $F_0 = 2$, the familiar neutral stability condition. Hence, superposed on the fine-scale flow structure, there is a propagating disturbance characterized by the travelling-wave coordinate, $\xi = x - 3t/2$.

Second, we decompose the fine-scale variation into two parts:

$$U_2 = \hat{U}_2(\eta) + \check{U}_2(\eta)u_1(\xi, \tau), \quad H_2 = \hat{H}_2(\eta) + \check{H}_2(\eta)u_1(\xi, \tau), \tag{5.14}$$

with

$$4\hat{U}_{2\eta} + \hat{H}_{2\eta} - \nu_1 \hat{U}_{2\eta\eta} = -4ff_\eta - 3f - 4F_1 f_\eta - \nu_1\left(f_\eta^2 - \overline{f_\eta^2}\right), \tag{5.15}$$
$$\hat{U}_{2\eta} + \hat{H}_{2\eta} = 2ff_\eta - \nu_1 f_\eta \overline{f_\eta^2}, \tag{5.16}$$
$$4\check{U}_{2\eta} + \check{H}_{2\eta} - \nu_1 \check{U}_{2\eta\eta} = -4f_\eta \tag{5.17}$$
$$\check{U}_{2\eta} + \check{H}_{2\eta} = -f_\eta. \tag{5.18}$$

The solution $\hat{U}_2$ and $\hat{H}_2$ represents a correction to the fine-scale flow structure, and is not needed for the evolution equation of the disturbance. The other component of

the solution can again be determined by decomposition into Fourier series:

$$\check{U}_2 = \sum_{j=1}^{\infty} \check{U}_j e^{ij\eta} + \text{c.c.}, \quad \check{H}_2 = \sum_{j=1}^{\infty} \check{H}_j e^{ij\eta} + \text{c.c.}, \quad (5.19)$$

with

$$\check{U}_j = -\frac{3 f_j e^{i\theta_j}}{\sqrt{9 + v_1^2 j^2}} \equiv \frac{3 A_j e^{2i\theta_j}}{9 + v_1^2 j^2}, \quad \check{H}_j = -\check{U}_j - f_j, \quad (5.20)$$

and $\tan \theta_j = v_1 j / 3$.

We proceed to one more order in $\epsilon$, where the spatially averaged equations are

$$h_{2\xi} - 2u_{2\xi} + 2u_2 - h_2 = 2F_1 u_{1\xi} - 4u_{1\tau} - 4u_1 u_{1\xi} - (u_1 - h_1)^2 - 4\overline{U_1^2}$$
$$+ v_1 \left[ u_{1\xi\xi} + \overline{(H_{2\eta} - U_{2\eta})U_{1\eta} + (h_1 - U_1)U_{1\eta}^2} \right], \quad (5.21)$$

$$\tfrac{1}{2} h_{2\xi} - u_{2\xi} = h_{1\tau} + (u_1 h_1)_\xi. \quad (5.22)$$

Finally, we eliminate the combination, $2u_2 - h_2$, to arrive at the evolution equation of our first expansion:

$$4u_{1\tau} + 3(u_1^2)_\xi - 8u_{1\tau\xi} - 6(u_1^2)_{\xi\xi} + v_1 \left( \overline{f_\eta^2} - 2\overline{\check{U}_{2\eta} f_\eta} \right) u_{1\xi}$$
$$+ 2\left( F_1 - v_1 \overline{f_\eta^2} \right) u_{1\xi\xi} + v_1 u_{1\xi\xi\xi} = 0. \quad (5.23)$$

## 5.2. *A second expansion; $v \sim \epsilon^2$ (theory B)*

A distinctive feature of the expansion above is that if $v_1 = 0$, topographic effects disappear entirely. In other words, terms representing 'inviscid' topographic effects must lie at higher order. To uncover these terms, we design a different expansion, with a smaller scaling for the viscosity. We sketch the alternative procedure: again we take $\epsilon \equiv k_b^{-1} \ll 1$ and $\zeta \to \epsilon A(\eta)$. This time the slow time scale is even slower, $\tau = \epsilon^2 t$, and we pose

$$v = \epsilon^2 v_2, \quad F = F_0 + \epsilon^2 F_2, \quad (5.24)$$

and the asymptotic sequences,

$$u = 1 + \epsilon U_1(\eta) + \epsilon^2 [U_2(\eta) + u_2(x, t, \tau)] + \epsilon^3 [U_3(\eta, x, t, \tau) + u_3(x, t, \tau)] + \dots,$$
$$h = 1 + \epsilon H_1(\eta) + \epsilon^2 [H_2(\eta) + h_2(x, t, \tau)] + \epsilon^3 [H_3(\eta, x, t, \tau) + h_3(x, t, \tau)] + \dots.$$

The corrections, $U_1$, $H_1$, $U_2$ and $H_2$, denote the fine-scale corrections due to the topography, whereas $u_2$ and $h_2$ now represent the growing disturbance.

The expansion proceeds much as before. A summary of the details is relegated to Appendix A. The principal result is the amplitude equation,

$$4u_{2\tau} + 3(u_2^2)_\xi - 8u_{2\tau\xi} - 6(u_2^2)_{\xi\xi} + 3\left( 6\overline{U_1^2} + v_2 \overline{U_{1\eta}^2} \right) u_{2\xi}$$
$$+ 2\left( F_2 - 3\overline{U_1^2} - v_2 \overline{U_{1\eta}^2} \right) u_{2\xi\xi} + v_2 u_{2\xi\xi\xi} = 0, \quad (5.25)$$

which explicitly contains the inviscid topography effects via the leading-order equilibrium correction, $U_1 = -A/3$.

## 5.3. *Revisiting linear stability*

We now revisit linear stability using the amplitude equations for the St. Venant model (equations (5.23) and (5.25)) by taking $u_j = v e^{iK\xi + \lambda\tau}$, with $j = 1$ or 2, and linearizing

in the perturbation amplitude $\upsilon$:

$$\lambda = \frac{K^2 q - iK(p - \nu_j K^2)}{4(1 - 2iK)}, \tag{5.26}$$

where

$$p = \begin{cases} \nu_1(\overline{f_\eta^2} - 2\overline{\check{U}_{2\eta} f_\eta}) \\ 3(6\overline{U_1^2} + \nu_2 \overline{U_{1\eta}^2}), \end{cases} \quad q = \begin{cases} 2(F_1 - \nu_1 \overline{f_\eta^2}) & \text{(theory A)} \\ 2(F_2 - 3\overline{U_1^2} - \nu_2 \overline{U_{1\eta}^2}) & \text{(theory B)}. \end{cases} \tag{5.27}$$

The growth rate is

$$\mathrm{Re}(\lambda) = \frac{K^2(q + 2p - 2\nu_j K^2)}{4(1 + 4K^2)}, \tag{5.28}$$

implying instability for $q + 2p > 0$. The neutral stability condition, $q + 2p = 0$, is written out fully as

$$F_1 = 2\nu_1 \overline{\check{U}_{2\eta} f_\eta} \quad \text{or} \quad F_2 = -15\overline{U_1^2} - 2\nu_2 \overline{U_{1\eta}^2}. \tag{5.29}$$

In both cases the critical Froude number is reduced by the topography (the corrections $F_1$ and $F_2$ are negative). To see this for theory A, we introduce the Fourier decompositions in (5.8) and (5.19), to find

$$F_1 = -36\nu_1 \sum_{j=1}^{\infty} \frac{j^2 |A_j|^2}{(9 + \nu_1^2 j^2)^2}. \tag{5.30}$$

Thus small-amplitude topography is destabilizing for any periodic profile.

On restoring the original variables, we find that the stability boundary near $(a, F) = (0, 2)$ is given by

$$F - 2 = \begin{cases} -36 k_b^2 \nu \sum_{j=1}^{\infty} j^2 |\zeta_j|^2 (9 + \nu^2 j^2 k_b^2)^{-2} & \text{for} \quad \nu \sim O(k_b^{-1}) \\ -(15\overline{\zeta^2} + 2\nu \overline{\zeta_\eta^2})/9 & \text{for} \quad \nu \sim O(k_b^{-2}), \end{cases} \tag{5.31}$$

where $A_j = k_b \zeta_j$ and $\zeta_j$ denotes the unscaled Fourier mode amplitudes of $\zeta(x)$. For the sinusoidal profile, $\zeta = a \sin(k_b x)$, the mode amplitudes are $\zeta_j = -ia\delta_{j1}/2$. It follows that

$$F - 2 = \begin{cases} -9\nu k_b^2 a^2 (9 + \nu^2 k_b^2)^{-2} & \text{for} \quad \nu \sim O(k_b^{-1}) \\ -(15 + 2\nu k_b^2) a^2/18 & \text{for} \quad \nu \sim O(k_b^{-2}). \end{cases} \tag{5.32}$$

These predictions are compared with numerical solutions of the linear stability problem in figures 8–10. Both versions of the asymptotics are used in the comparison, choosing one or the other according to the size of $\nu$. In figure 10 the stability boundary is shown over a range of $\nu$; the numerical results span both ranges of the asymptotics, $\nu \sim k_b^{-1}$ and $k_b^{-2}$, and there is a distinctive crossover between the two asymptotic predictions for intermediate values of $\nu$.

### 5.4. *Canonical form*

With periodic boundary conditions, the amplitude equation has the property that Galilean transformations cause a constant shift in $u_j$. This allows us to place the amplitude equation into a canonical form by defining a new variable, $\varphi = 3u_j/2 + C$, and introducing a coordinate transformation, $(\xi, \tau) \to (\xi', \tau) = (\xi + c\tau, \tau)$. We may

then eliminate any correction to the background equilibrium profile using $C$, and remove the term $qu_{j\xi\xi}$ by suitably selecting the frame speed $c$. The result is our final amplitude equation,

$$(1 - 2\partial_\xi)(\varphi_\tau + \varphi\varphi_\xi) + p\varphi_\xi + \mu\varphi_{\xi\xi\xi} = 0, \quad (5.33)$$

which has the two parameters $p$ and $\mu = \nu_j/4$, and the unique equilibrium state, $\varphi = 0$. A third parameter is the domain size in which we solve the equation, $d$. If we scale time and amplitude, $\tau \to \tau/|p|$ and $\varphi \to |p|\varphi$, we may further set the parameter $p$ to $\pm 1$, leaving only $\mu$ and $d$ as parameters. Below we present some numerical solutions of the amplitude equation; we exploit this final scaling to put $p = 1$, focusing only on unstable flows.

The amplitude equation (5.33) is identical in form to reduced models derived by Yu & Kevorkian (1992) and Kevorkian *et al.* (1995). An additional short-wave approximation leads to the modified Burgers equation derived by Kranenburg (1992), whilst a long-wave approximation gives a generalized Kuramoto–Sivashinsky equation, as considered by Yu *et al.* (2000). In contrast to those two final models, (5.33) correctly describes both long and short waves (which can be verified by looking at linear stability – Mandre 2001). Yu *et al.* (2000) and Kevorkian *et al.* (1995) used a slightly different form for the diffusive term at the outset. Consequently, some of the coefficients in (5.33) differ from those of the corresponding amplitude equations of Yu *et al.* when compared in the appropriate limit. This reflects the extent to which the amplitude equation depends on the form of the diffusion term.

## 6. Nonlinear roll-wave dynamics

In this section, we explore the nonlinear dynamics of roll waves, solving numerically both the shallow-water model (and, in particular, the St. Venant version) and the amplitude equation derived above. Related computations have been reported previously by Kranenburg (1992), Kevorkian *et al.* (1995), Brook, Pedley & Falle (1999) and Chang *et al.* (2000), who ignored bottom topography and gave an incomplete picture of the selection of wavelengths of nonlinear roll waves.

### 6.1. *St. Venant model*

We numerically integrated the St. Venant model with sinusoidal topography, beginning from the initial conditions, $uh = 1$ and $h = 1$. A pseudo-spectral discretization in space and a fourth-order Runge–Kutta time-stepping scheme was used. A sample integration is shown in figure 13. In this run, the system falls into the eye of instability of §4, and the domain contains ten wiggles of the background topography. The short-scale effect of the topography is evident in $h$, but is far less obvious in the flux, which makes $hu$ a convenient variable to visualize the instability. In figure 13, the instability grows from low amplitude and then saturates to create a steadily propagating nonlinear roll wave (modulo the periodic variation induced as the wave travels over the topography). Although the run in figure 13 lies in the eye of instability, similar results are obtained elsewhere in parameter space: figure 14 shows results from a run nearer the classical roll-wave regime.

We define a measure of the roll-wave amplitude by

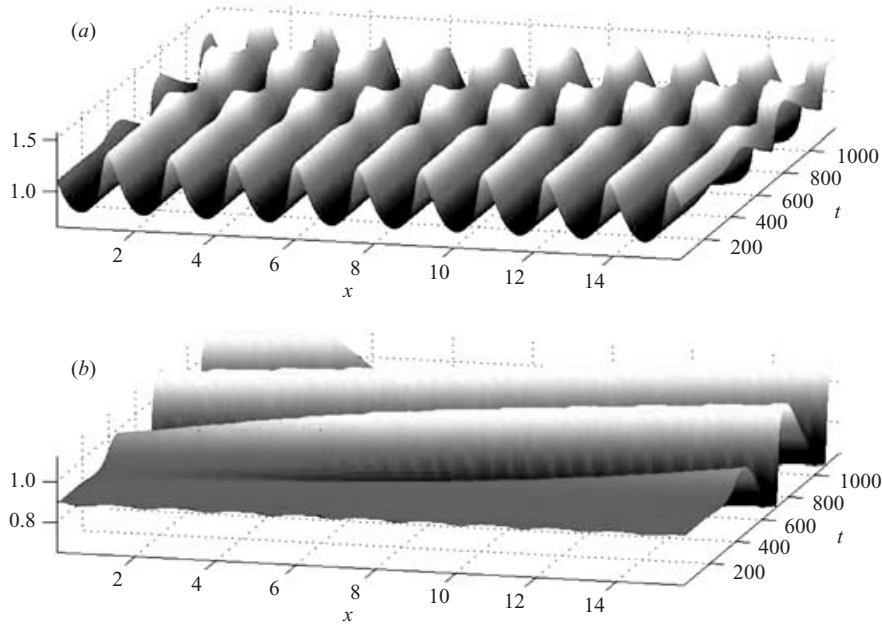$$I^2(t) = \int_0^L (uh - \langle uh \rangle)^2 \mathrm{d}x, \quad (6.1)$$

FIGURE 13. A numerical solution of the St. Venant model with $F = 1.58$, $v = 0.05$, $a = 0.32$ and $k_b = 4$. The domain has size $5\pi$. (a) $h(x, t)$, and (b) the flux, $hu$, as surfaces above the $(x, t)$-plane. The solution is 'strobed' every 11 time units in order to remove most of the relatively fast propagation of the instability (and make the picture clearer).
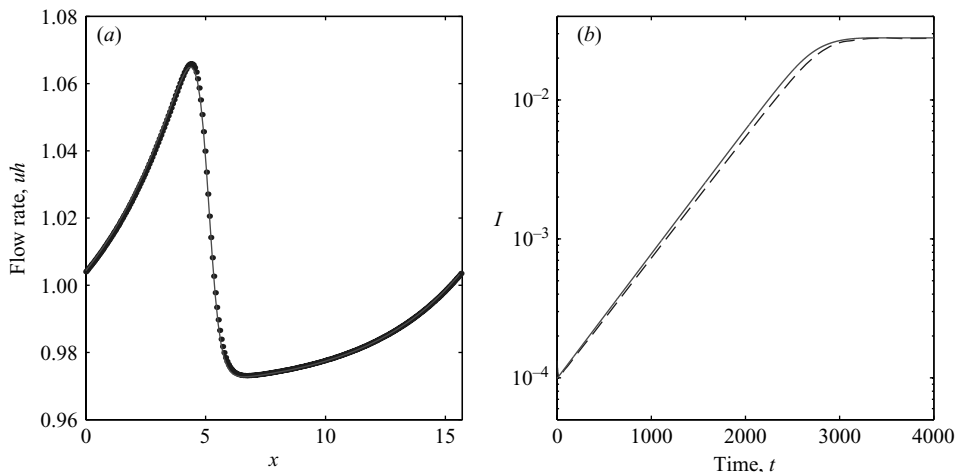


FIGURE 14. (a) The flux ($uh$) associated with a nonlinear roll wave, computed from the St. Venant model (dots) and reconstructed from the amplitude equation (solid line), for $v = 0.05$, $F = 2.05$, $a = 0.03$ and $k_b = 4$. (b) The corresponding evolution of the saturation measure, $I(t)$, for the amplitude equation (solid line) and St. Venant model (dashed line).

where $\langle uh \rangle$ denotes the spatial average of the flux. As illustrated in figure 14, this quantity can be used to monitor saturation. Figure 15 shows the saturation amplitude as a function of the Froude number for $a = 0.3$, $v = 0.05$ and $k_b = 10$. This slice through the $(a, F)$-parameter plane intersects the eye of instability at smaller Froude
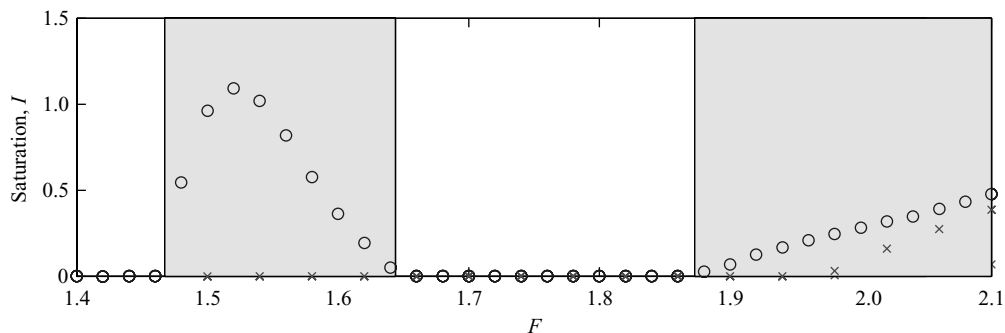
FIGURE 15. Saturation amplitudes for the shallow-water equations (circles) for $k_b = 4$, $K = 0.2$, $\nu = 0.05$ and $a = 0.3$. The shaded region shows the range of linear instability of the steady background flow. Corresponding results from the amplitude equation (crosses) are also shown for comparison.

number as well as Jeffrey's threshold. At each stability boundary, the saturation level declines smoothly to zero, and so we conclude that the bifurcation to instability is supercritical.

## 6.2. Amplitude equation

Figure 14 also includes a numerical solution of our amplitude equation for comparison with that from the St. Venant model. The numerical method employed a pseudo-spectral scheme in space and a Gear-type time-integrator. The asymptotic scalings have been used to match parameter settings and reconstruct the solution in terms of the original variables. Each of the computations begins with small perturbations about the equilibrium flow, although transients not captured by the asymptotic theory preclude agreement over a brief initial period. To remove that transient and improve the comparison of the longer-time dynamics, we have offset the asymptotic solution in time. Figure 14 illustrates what appears to be the general result that the amplitude equation (5.33) faithfully reproduces the roll-wave dynamics of the St. Venant model (see also figure 15, which shows qualitative agreement in the saturation measure near $F = 2$, despite a relatively large topographic amplitude). We therefore focus on the amplitude equation in giving a fuller discussion of the roll-wave dynamics, thereby avoiding separate discussions of the problem with and without bottom topography.

Figure 16 shows the evolution of a typical roll-wave pattern, and illustrates a key result found by previous authors – namely that roll waves coarsen. The simulation starts from an initial condition consisting of low-amplitude, rapidly varying perturbations about the uniform equilibrium state, $\varphi = 0$. The instability grows and steepens into about eight non-identical roll waves. These waves propagate at different speeds, causing some of them to approach and collide. The colliding waves then merge into larger waves, a process that increases the length scale of the wave train. The collisions continually recur to create an inverse cascade that eventually leaves a pattern with the largest possible spatial scale, a single (periodic) roll wave. Coarsening has been observed in many different physical systems, and the dynamics seen in figure 16 seems, at first sight, to be no exception.

Coarsening dynamics can be rationalized, in part, in terms of the subharmonic instability of trains of multiple roll waves. Specially engineered initial-value problems illustrate this notion quantitatively. For example, figure 17 shows the response of two periodic wave trains to subharmonic perturbations. The two simulations begin
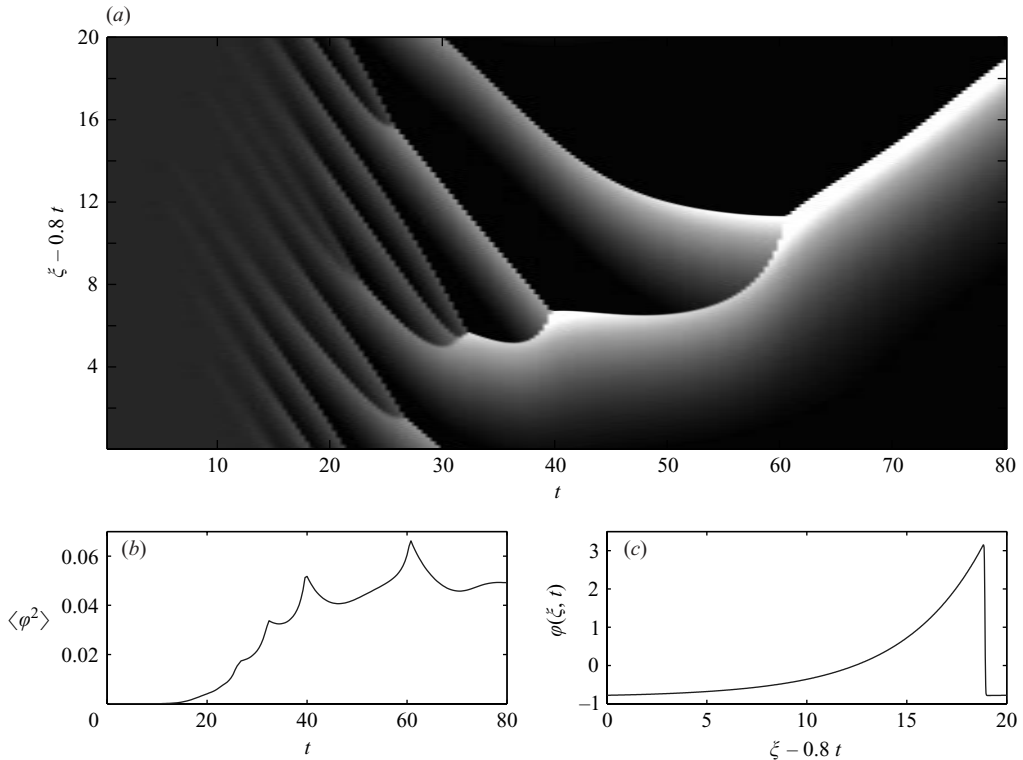
FIGURE 16. Coarsening of roll waves predicted by the amplitude equation (5.33) for $d = 20$ and $\mu = 0.05$. (a) $\varphi(\xi, t)$ as a density on the $(t, \xi)$-plane. (b), (c) The amplitude measure $\langle \varphi^2 \rangle$ (the spatial average of $\varphi^2$) and final profile. The initial condition consisted of about eleven low-amplitude irregular oscillations.

with initial conditions dominated by wavenumber four and six, respectively, but also contain subharmonic wavenumbers with much lower amplitude. In each case, a train of waves appears that propagates steadily for a period. Somewhat later, the small subharmonic perturbations of the basic disturbance prompt collisions to trains with half the number of waves. Again, these trains persist for a period, but then final mergers occur to leave a single roll wave. We interpret the growth of subharmonic perturbations in figure 1(c) to be the analogue of this instability.

Despite the total coarsening evident in figures 16 and 17, we have also found that roll waves do not always complete an inverse cascade. Exploring a little, we find parameters for which periodic trains of multiple roll waves appear to be stable. Figure 18 shows such an example: a stable train of two roll waves emerges after a number of mergers. Thus coarsening does not always continue to its final conclusion, but becomes interrupted at an intermediate scale. We have verified that this is also a feature of the St. Venant problem.

### 6.3. *Linear stability of roll waves*

The limitations of the coarsening dynamics can be better quantified with a linear stability analysis of periodic nonlinear roll-wave trains. Those steadily propagating solutions take the form $\varphi = \Phi(\xi - c\tau)$, where $c$ is the wave speed, and satisfy

$$\tfrac{1}{2}(1 - 2\partial_\xi)[(\Phi - c)^2]_\xi + \Phi_\xi + \mu \Phi_{\xi\xi\xi} = 0. \tag{6.2}$$
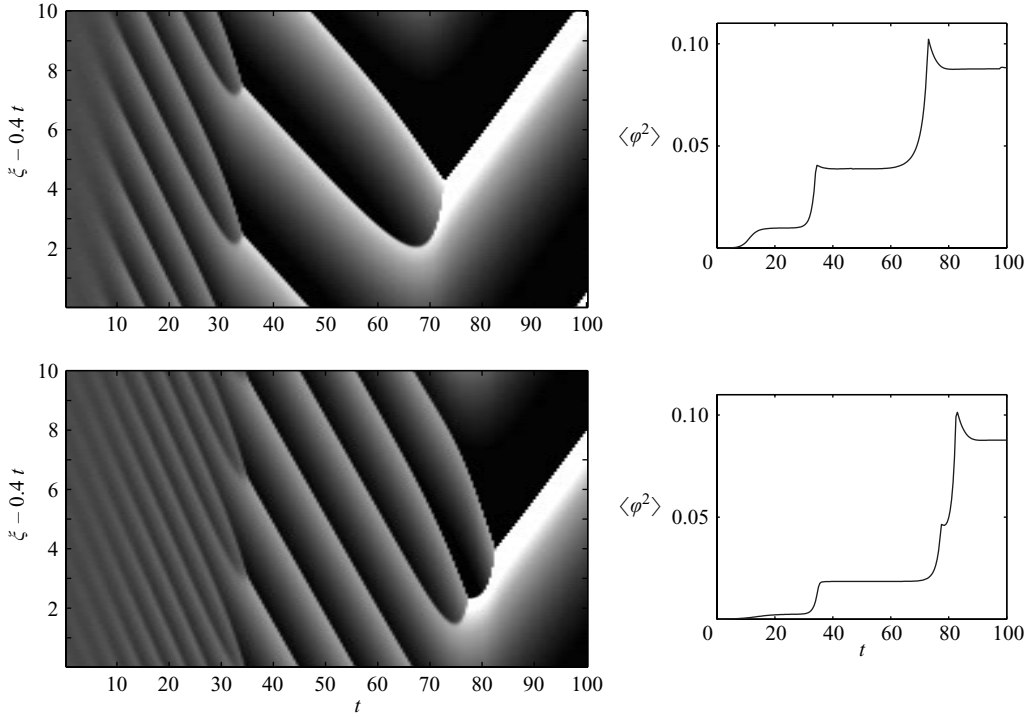
FIGURE 17. Coarsening dynamics as a subharmonic instability of steady roll-wave trains, for $\mu = 0.05$, and in a domain of length 10.
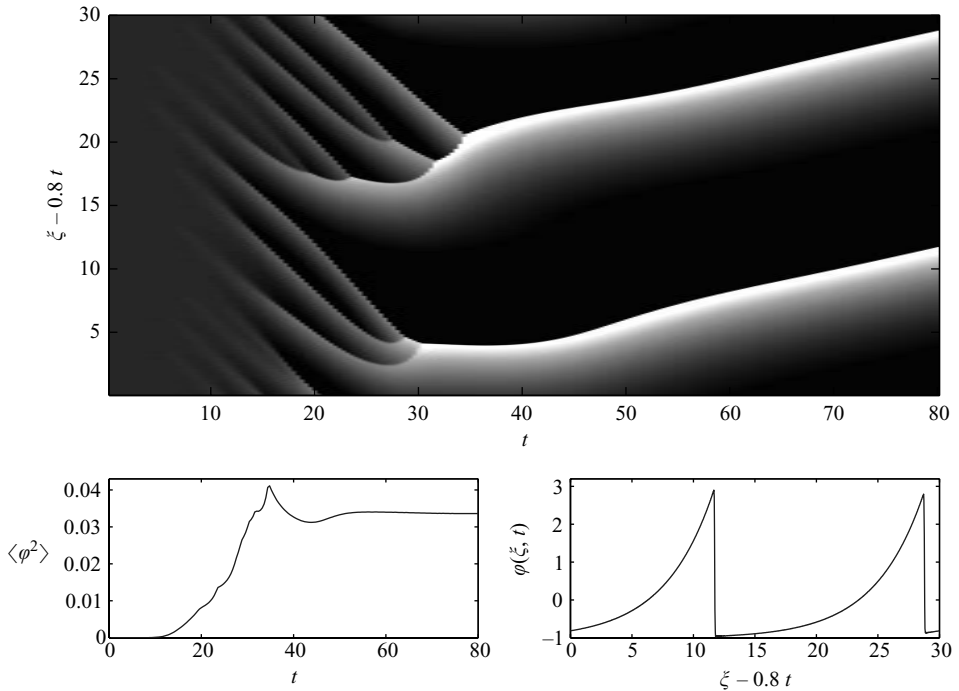


FIGURE 18. A picture similar to figure 16 showing interrupted coarsening for $\mu = 0.05$ in a domain of length 30 (and similar initial condition).
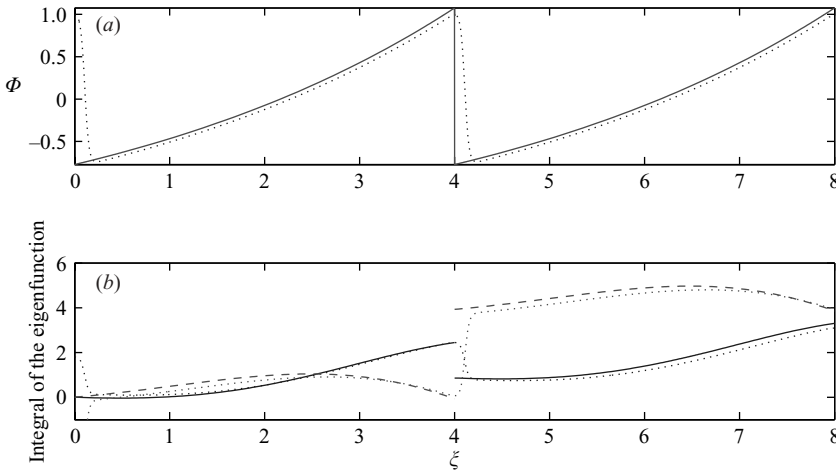
FIGURE 19. (a) Steadily propagating roll-wave solutions of the amplitude equation for $L = 4$ and $\mu = 0.04$ (dotted) and $\mu = 0$ (solid). (b) The real (solid) and imaginary (dashed) parts of an unstable eigenfunction with twice the spatial period as the basic roll wave. We use the integral of $\hat{\varphi}$ to display the eigenfunction because $\hat{\varphi}$ itself contains a delta function related to the movement of the shock for $\mu = 0$, or a large-amplitude spike for $\mu = 0.04$ which obscures the picture. The eigenvalue is $\sigma = 0.2390$.

Auxiliary conditions on $\Phi$ are periodicity, the choice of origin (equation (6.2) is translationally invariant) and the integral constraint,

$$\int_0^L \Phi(s) \, ds = 0 \tag{6.3}$$

(which follows from the fact that this integral is a constant of motion for (5.33) and vanishes for the specified initial condition). This system can be solved numerically; a sample solution is shown in figure 19.

An analytical solution to (6.2) is possible in the inviscid case: After requiring regularity at the singular point, $\Phi = c$, we find

$$\Phi(\xi - c\tau) = A \exp\left(\frac{\xi - c\tau}{4}\right) + c - 2 \tag{6.4}$$

where $A$ is a constant of integration. Because (6.4) is a monotonic function, a shock must be placed in the solution with jump condition

$$c = \frac{\Phi_+ + \Phi_-}{2}, \tag{6.5}$$

where subscripts denote the value of $\Phi$ upstream and downstream of the shock. After imposing the remaining auxiliary conditions, we find

$$A = 4/\left(e^{L/4} + 1\right), \quad c = 2 - \frac{16}{L} \tan h\left(\frac{L}{8}\right). \tag{6.6}$$

This solution is compared with the weakly viscous solution of (6.2) in figure 19.

To study the stability of the steady solutions, we introduce $\varphi(\xi, \tau) = \Phi(\xi - c\tau) + \hat{\varphi}(\xi - c\tau)e^{\sigma\tau}$ into (5.33) and linearize in the perturbation amplitude $\hat{\varphi}(\xi - c\tau)$:

$$\sigma \hat{\varphi} - \tfrac{1}{2}\hat{\varphi} + [(\Phi - c)\hat{\varphi}]_\xi = \psi, \tag{6.7}$$

$$(2\partial_\xi - 1)\psi - \tfrac{1}{2}\hat{\varphi} - \mu\hat{\varphi}_{\xi\xi\xi} = 0, \tag{6.8}$$

with $\psi$ an auxiliary variable and $\sigma$ the sought growth rate. The solution proceeds by introducing another Bloch wavenumber, $K$, to gauge stability with respect to perturbations with longer spatial scale than the steady wave train. Numerical computations then provide the growth rate, $\mathrm{Re}(\sigma)$, as a function of $K$; an example eigenfunction of the weakly viscous solution is also displayed in figure 19(b).

In the inviscid problem, the stability theory is complicated by the shock, which, in general, shifts in space under any perturbation. The shifted shock contributes a delta function to the linear solution. We take this singular component into account using suitable jump conditions: integrating (6.7) and (6.8) with $\mu = 0$ across the discontinuity, and allowing for an arbitrary delta-function of amplitude $\Delta$ in $\hat{\varphi}$, gives

$$\left(\sigma - \tfrac{1}{2}\right)\Delta + (\Phi^+ - c)(\hat{\varphi}^+ + \hat{\varphi}^-) = \psi \tag{6.9}$$

$$\psi^+ - \psi^- = \tfrac{1}{4}\Delta. \tag{6.10}$$

A boundary-layer analysis based on the weakly viscous stability problem provides exactly these relations, except as matching conditions across the boundary layer. The regularity condition, $\psi = \sigma\hat{\varphi}$, must also be imposed at the singular point, $\Phi = c$. Despite the lower order of the linear stability problem, an analytical solution is not possible and we again solve the system numerically. Figure 19 once more compares inviscid and weakly viscous solutions.

Typical results for the dependence of the growth rate of the most unstable mode on wave spacing, $L$, are shown in figure 20. Four values of the Bloch wavenumber are shown, corresponding to steady wave trains with $n = 1$, 2, 3 and 4 waves, each a distance $L$ apart, in a periodic domain of length $nL$. As we increase the wave spacing, there is a critical value beyond which periodic trains with multiple waves become stable. This stabilization of multi-wave trains applies to general values of $K$ and $\mu$, as illustrated by the neutral stability curves shown in figure 21. Thus, wave trains with sufficiently wide spacing become stable to subharmonic perturbations, removing any necessity for coarsening.

Figures 20 and 21 also illustrate that at yet larger wave spacing, a different instability appears which destabilizes a single roll wave in a periodic box ($n = 1$). For these wavelengths, the nonlinear wave develops a long flat tail resembling the unstable uniform flow. Hence, we interpret the large-$L$ instability as resulting from perturbations growing on that plateau. We verify this character of the instability by solving the amplitude equation numerically, beginning from an initial condition close to the unstable nonlinear wave. Figure 22 illustrates how small disturbances grow and disrupt the original wave; eventually further peaks appear and four roll waves are present by the end of the computation, of which two are about to merge. Later still, the system converges to a steady train of three waves. In other words, trains with spacings that are too wide suffer wave-spawning instabilities that generate wave trains with narrower separations.

The combination of the destabilization of trains of multiple waves at lower spacing and the wave-spawning instability at higher spacing provides a wavelength selection mechanism for nonlinear roll waves. We illustrate this selection mechanism further in figure 23, which shows the results of many initial value problems covering a range of domain lengths, $d$. Each computation begins with a low-amplitude initial condition with relatively rapid and irregular spatial variation. The figure catalogues the final wave spacing and displays the range over which trains of a given wave separation are linearly stable. Also shown is the wavelength of the most unstable linear eigenmode of
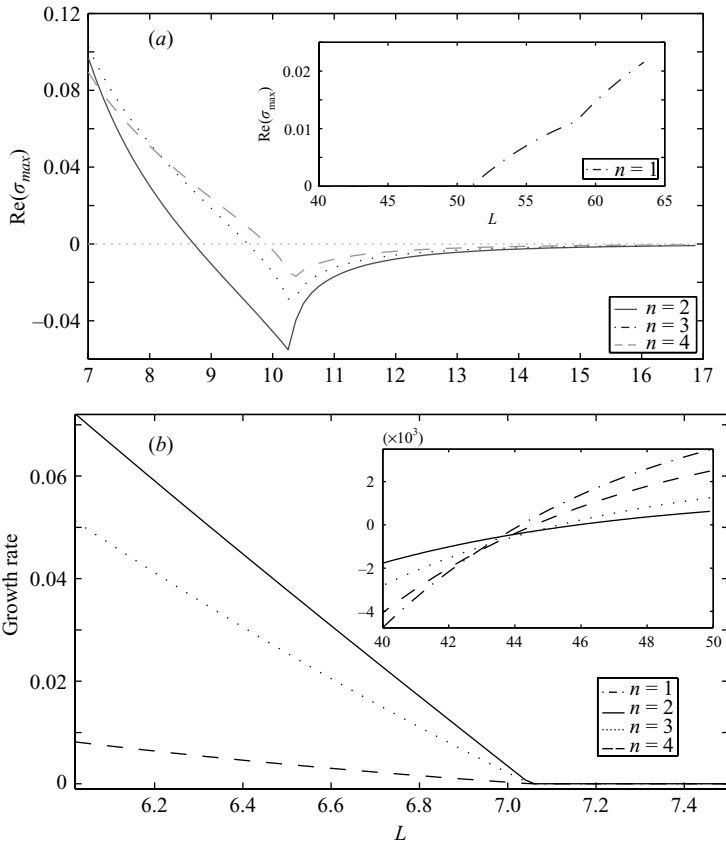
FIGURE 20. Linear stability results of roll waves using the amplitude equation for $\mu = 1$ (*a*) and $\mu = 0$ (*b*). Growth rate is plotted against wave spacing ($L$) for perturbations having a Bloch wavenumber of $K = 2\pi/nL$ (except for $n = 1$, where $K = 0$.)
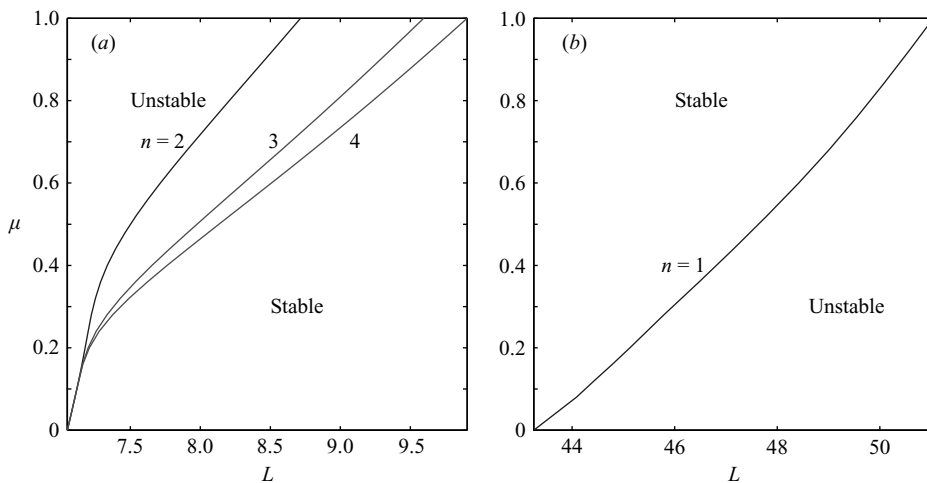


FIGURE 21. Stability boundaries for nonlinear roll waves on the $(L, \mu)$-plane. (*a*) The stability curves for $n = 2$, 3 and 4 (corresponding to roll-wave trains with $n$ peaks in a periodic domain of size $nL$). (*b*) The stability boundary for a single roll wave in much longer periodic domains.
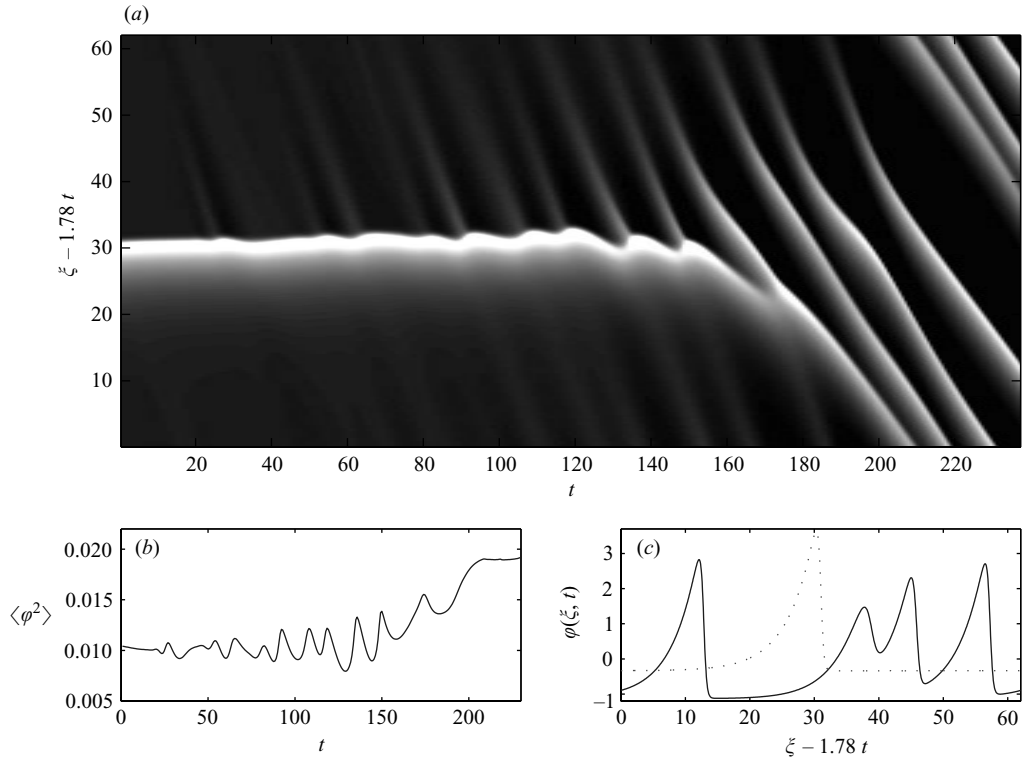
FIGURE 22. A solution of the amplitude equation, beginning with an initial condition near an unstable roll wave. ($L = 62$ and $\mu = 1$). The dotted line in (*c*) shows the initial condition.

the uniform equilibrium, which typically outruns the other unstable modes to create a first nonlinear structure in the domain. At lower viscosities ($\mu$), the most unstable mode is too short to be stable, and the inception of the associated nonlinear wave is followed by coarsening until the wave separation falls into the stable range. As we raise $\mu$, however, the most unstable mode falls into the stable range, and the nonlinear wave trains that appear first remain stable and show no coarsening. Thus, viscosity can arrest coarsening altogether.

## 7. Discussion

In this article, we have investigated turbulent roll waves in flows down planes with topography. We combined numerical computations of both the linear and nonlinear problems with an asymptotic analysis in the vicinity of the onset of instability. The results paint a coherent picture of the roll-wave dynamics.

The addition of low-amplitude bottom topography tends to destabilize turbulent flows towards long-wave perturbations, depressing the stability boundary to smaller Froude number. At moderate topographic amplitudes, an eye of instability also appears at much smaller Froude number, a feature connected to the development of topographically induced hydraulic jumps in the background equilibrium flow (at least for the St. Venant model). At larger amplitudes, the topography appears to be stabilizing, and the onset of roll waves occurs at higher Froude numbers than expected for a flat bottom. This is consistent with observations of hydraulic engineers, who
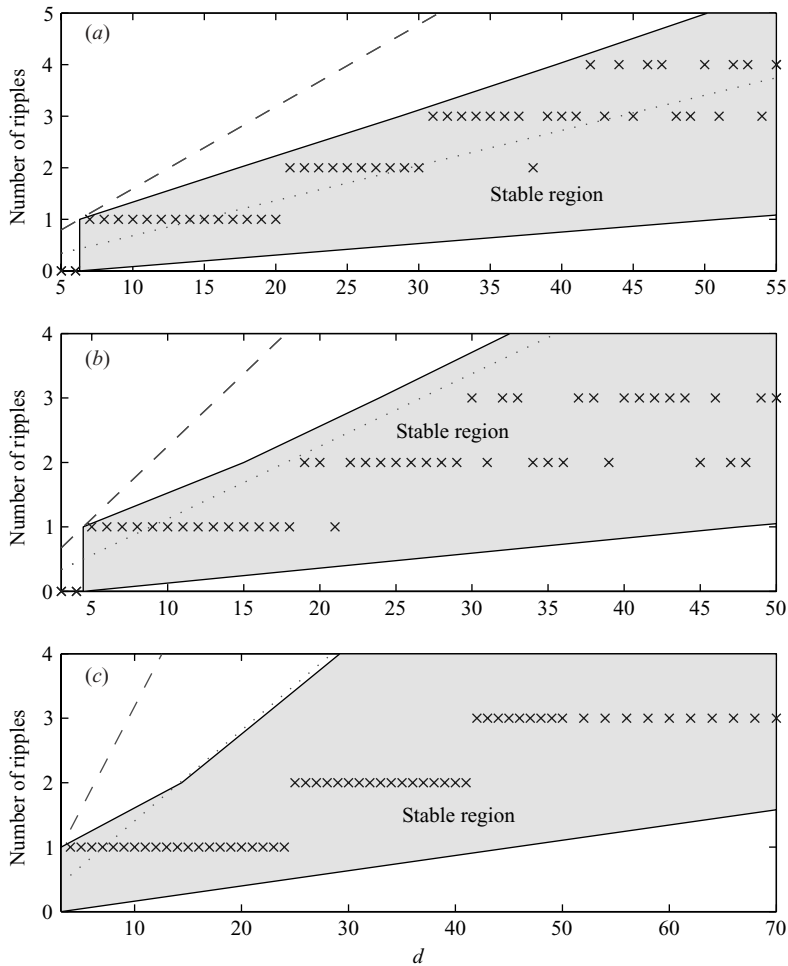
FIGURE 23. Final roll-wave spacings (crosses) in a suite of initial-value problems with varying domain size $d$ and three values of $\mu$: (*a*) 1, (*b*) 0.5, (*c*) 0.25. The shaded region shows where nonlinear wave trains are linearly stable. Also shown are the stability boundaries of the uniform flow (dashed line) and the fastest growing linear mode from that equilibrium (dotted line).

traditionally have exploited structure in the bed to eliminate roll waves in artificial water conduits, although usually in the direction transverse to the flow (Rouse 1938; Montes 1998).

We have also found that the reduced model furnished by asymptotic theory faithfully reproduces the nonlinear dynamics of roll waves. The model indicates that roll waves proceed through an inverse cascade due to coarsening by wave mergers, as found previously (Kranenburg 1992; Yu & Kevorkian 1992; Chang *et al.* 2000). This phenomenon was also observed in the experiments conducted by Brock (1969). However, the cascade does not continue to the longest spatial scale, but instead becomes interrupted over intermediate wavelengths. Moreover, wave trains with longer scale are unstable to wave-nucleation events. Thus, roll-wave trains emerge with a range of selected spatial scales. In ongoing research, we plan to
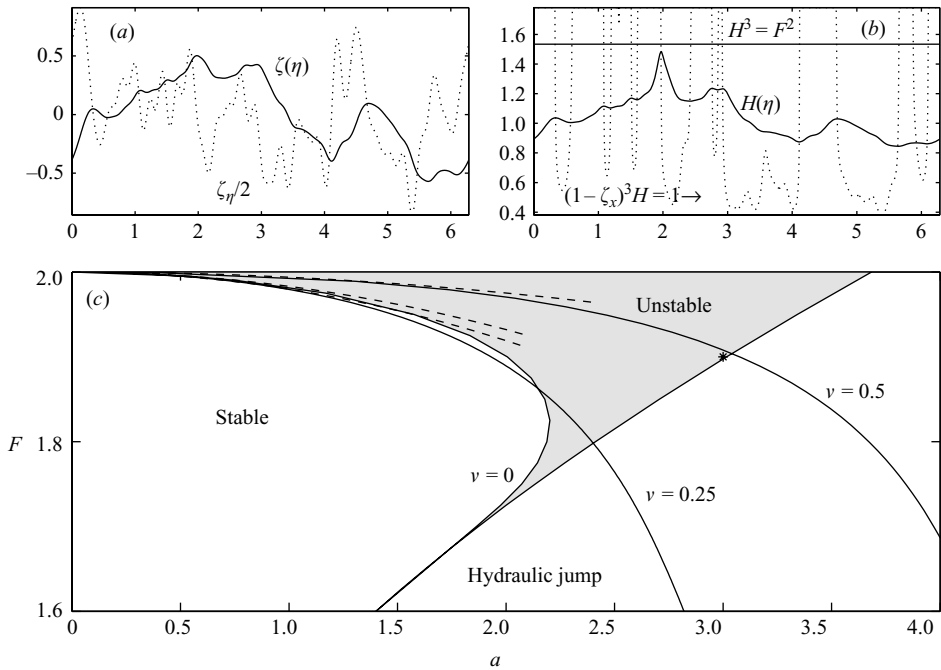
FIGURE 24. A computation with 'random' topography. (*a*) The realization of the topography and its derivative, constructed as follows: $\zeta$ is built from a Fourier series in which real and imaginary parts of the amplitude, $\zeta_n$, are drawn randomly from normal probability distributions with zero mean and standard deviation, $(n^2 + 16)^{-5/4}$, for $n = 1, 2, \ldots, 32$, and then a reality condition is imposed. (*b*) The inviscid equilibrium for $a = 3$, $k_b = 10$ and $F = 1.9$, together with the organizing curves, $H^3 = F^2$ and $(1 - \zeta_x)H^3 = 1$; the solution is about to form a hydraulic jump (and is marked by a star in (*c*)). (*c*) The (shaded) instability region on the $(a, F)$-plane for $\nu = 0$; to the right of this region, the periodic equilibria cease to exist, and weakly viscous solutions develop hydraulic jumps. Also indicated are the viscous stability boundaries for $\nu = 0.25$ and $0.5$; viscous equilibria are unstable above this curve. The dashed lines show the corresponding stability boundaries predicted by asymptotics (with theory A for $\nu = 0.25$ and $0.5$ and theory B for $\nu = 0$).

continue experiments like that shown in figure 1 to verify this wavelength selection process further.

Although our results for low-amplitude topograpy are quite general, the discussion of instabilities caused by the hydraulic jump has centred on a sinusoidal topographic profile and one may wonder how the results differ when the bed is more complicated. To answer this question we have made further explorations of the linear stability problem with a less regular form for $\zeta$. In particular, we have tested the linear stability of equilibria flowing over 'random topography'. Here, $\zeta$ is constructed using a Fourier series representation; the coefficients of the series are chosen randomly from a normal distribution whose mean and standard deviations depend on the order of the Fourier mode. In this way, the topography conforms to a specific spectral distribution, as sometimes used in descriptions of the ocean's floor (Balmforth, Ierley & Young 2002). An example is shown in figure 24, which displays the realization of $\zeta$, an inviscid equilibrium solution on the $(\eta, H)$ phase plane, and inviscid and weakly viscous stability boundaries on the $(F, a)$-plane. The overall conclusions are much the same as for the sinusoidal case: the inclusion of topography lowers the stability

boundary below $F = 2$, and there is a significant destabilization associated with the formation of hydraulic jumps in the equilibrium.

We close by remarking on the application of our results. We have considered shallow-water equations with drag and viscosity, focusing mostly on the St. Venant parametrization for turbulent flows and briefly on the Shkadov model for laminar flows. We found that introduction of small, periodic, but otherwise arbitrary, topography destabilizes turbulent roll waves but stabilizes the laminar ones. For both kind of flows, the formation of a hydraulic jump in the equilibrium can further destabilize the flow (at least near the $F_2$-curve, if not near $F = F_1$), a feature that may play a role in other physical settings. For example, carefully fabricated periodic ribbing in the elastic wall of a conduit may promote instability in the related physiological and engineering problems. In contrast, our results on the nonlinear dynamics of roll waves are more general: whatever the underlying physical setting, they should apply equally.

## Appendix A. The second expansion

In the second expansion (theory B), we introduce

$$\partial_t \to \partial_t + \epsilon^2 \partial_\tau, \quad \partial_x \to \frac{1}{\epsilon}\partial_\eta + \partial_x, \quad \nu = \epsilon^2 \nu_2, \quad F = F_0 + \epsilon^2 F_2, \tag{A 1}$$

and

$$u = 1 + \epsilon U_1(\eta) + \epsilon^2[U_2(\eta) + u_2(x, t, \tau)] + \epsilon^3[U_3(\eta, x, t, \tau) + u_3(x, t, \tau)] + \dots,$$
$$h = 1 + \epsilon H_1(\eta) + \epsilon^2[H_2(\eta) + h_2(x, t, \tau)] + \epsilon^3[H_3(\eta, x, t, \tau) + h_3(x, t, \tau)] + \dots.$$

At leading order:

$$F_0^2 U_{1\eta} + H_{1\eta} + A_\eta = 0, \quad U_{1\eta} + H_{1\eta} = 0, \tag{A 2}$$

with solution

$$U_1 = -\frac{1}{F_0^2 - 1} A(\eta) \equiv -H_1. \tag{A 3}$$

At order $\epsilon^2$, we find inconsequential equilibrium corrections. At order $\epsilon^3$:

$$F_0^2 U_{3\eta} + H_{3\eta} = \nu_2 U_{2\eta\eta} - 2U_2 + H_2 - (U_1 - H_1)^2 + \nu_2 H_{1\eta} U_{1\eta} - F_0^2 (U_1 U_2)_\eta$$
$$- 2F_0 F_1 U_{1\eta} - F_0^2(u_{2t} + u_{2x}) - h_{2x} - 2u_2 + h_2 - F_0^2 U_{1\eta} u_2, \tag{A 4}$$

$$U_{3\eta} + H_{3\eta} = -(H_2 U_1 + H_1 U_2 + H_1 u_2 + h_2 U_1)_\eta - h_{2x} - u_{2x} - h_{2t}. \tag{A 5}$$

We average over the fine length scale $\eta$ to eliminate the corrections, $U_3$ and $H_3$:

$$F_0^2(u_{2t} + u_{2x}) + h_{2x} + 2u_2 - h_2 = -4\overline{U_1^2} - \nu_2 \overline{U_{1\eta}^2}, \quad h_{1t} + h_{1x} + u_{1x} = 0. \tag{A 6}$$
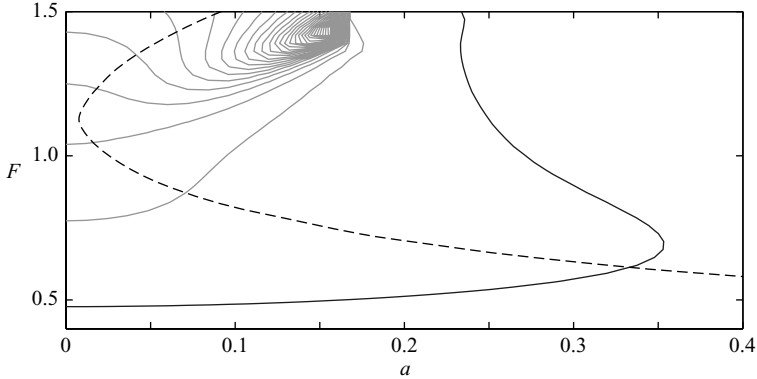
FIGURE 25. Contours of constant growth rate ($\sigma$) for $\nu = 0.02$, $k_b = 10$, $K = 10^{-3}$. Thirty equally spaced contours (dotted lines) are plotted with the growth rate going from $6.09 \times 10^{-5}$ to 0. The solid line denotes the neutral stability curve and the dashed line shows the location of $F_1$, $F_2$ and $F_*$ curve.

To avoid exponential growth along the characteristics we impose

$$h_2(\xi) = 2u_2(\xi) + \nu_2\overline{U_{1\eta}^2} + 4\overline{U_1^2} \equiv 2u_2(\xi) + \nu_2\overline{A_\eta^2} + 4\overline{A^2}, \tag{A 7}$$

and $F_0 = 2$. We decompose the fine-scale variation into two parts:

$$U_3 = \hat{U}_3(\eta) + \check{U}_3(\eta)u_2(\xi, \tau), \quad H_3 = \hat{H}_3(\eta) + \check{H}_3(\eta)u_2(\xi, \tau). \tag{A 8}$$

The solution, $\hat{U}_3$ and $\hat{H}_3$, is not needed. The other component satisfies

$$4\check{U}_{3\eta} + \check{H}_{3\eta} = -4U_{1\eta}, \quad \check{U}_{3\eta} + \check{H}_{3\eta} = -U_{1\eta}. \tag{A 9}$$

That is, $\check{H}_3 = 0$ and $\check{U}_3 = -U_1 = A/3$.

At orders $\epsilon^3$ and $\epsilon^4$, we arrive at equations for $H_4(\eta, x, t, \tau)$, $U_4(\eta, x, t, \tau)$, $H_5(\eta, x, t, \tau)$ and $U_5(\eta, x, t, \tau)$, which are not needed. We skip directly to the $\eta$-averaged equations at order $\epsilon^4$:

$$h_{4\xi} - 2u_{4\xi} + 2u_4 - h_4 = 2F_2u_{2\xi} - 4u_{2\tau} - 4u_2u_{2\xi} - (u_2 - h_2)^2 + 4\overline{U_1^2}(2h_2 - u_2)$$

$$+ \nu_2\overline{U_{1\eta}^2}h_2 + \nu_2u_{2\xi\xi} - 4\overline{U_1U_{3\xi}} + 4\overline{U_1(H_3 - U_3)} - 4\overline{U_1^4}$$

$$+ \nu_2\overline{U_{1\eta}(H_{3\eta} - U_{3\eta}) + H_{2\eta}U_{2\eta}} - 4\overline{U_1^2(U_2 - 2H_2)}$$

$$- \overline{(U_2 - H_2)^2} + \nu_2\overline{U_{1\eta}^2H_2} + \overline{(H_{2\eta} - U_{2\eta})U_{1\eta}U_1}, \tag{A 10}$$

$$h_{4\xi} - 2u_{4\xi} = 4u_{2\tau} + 2(h_2u_2)_\xi + 2\overline{(U_1H_{3\xi} + U_{3\xi}H_1)}. \tag{A 11}$$

Finally, we eliminate the combination, $2u_4 - h_4$, to arrive at (5.25).

## Appendix B. The laminar model

Throughout this article, we have used the turbulent drag law (1.3) to provide a closure to equations (1.1) and (1.2). Here we provide linear stability and asymptotic results using the laminar law (1.4).

Results from the linear stability analysis for the laminar problem reveal a slightly different picture than for the turbulent counterpart. As seen in figure 25, when topography is introduced, the critical Froude number is raised above $\sqrt{5/22}$, the

critical Froude number for a flat bottom in this case. In this sense, topography is stabilizing. The figure also shows a sharp spike in the linear growth rate, similar to that seen in figure 11. This spike is close to the $F_2$-curve and is reminiscent of the instability induced by the hydraulic jump in the turbulent case, except that it now occurs above the counterpart of Jeffrey's threshold.

We repeat the asymptotic analysis for the laminar model using scalings identical to the ones used for the turbulent problem. We provide here the final amplitude equations for both possible scalings. For theory A,

$$u_{1\tau} - \tfrac{21}{22}u_{1\tau\xi} + \tfrac{3}{2}(u_1^2)_\xi - \tfrac{15}{22}(u_1^2)_{\xi\xi} + 2\nu_1\big(\overline{f_\eta^2} - 2\overline{\check{U}_{2\eta}f_\eta}\big)u_{1\xi}$$
$$+ \big(2\sqrt{\tfrac{22}{5}}F_1 - \tfrac{1}{2}\nu_1\overline{f_\eta^2}\big)u_{1\xi\xi} + 2\nu_1 u_{1\xi\xi\xi} = 0, \quad \text{(B 1)}$$

where $f$ and $\check{U}_2$ satisfy

$$-\tfrac{9}{11}f - \nu_1 f_\eta + A = 0, \quad \text{(B 2)}$$
$$-\tfrac{9}{11}\check{U}_2 - \nu_1\check{U}_{2\eta} + \tfrac{15}{22}f = 0. \quad \text{(B 3)}$$

For theory B,

$$u_{2\tau} - \tfrac{21}{22}u_{2\xi\tau} - \tfrac{15}{22}(u_2^2)_{\xi\xi} + \tfrac{3}{2}(u_2^2)_\xi + \big(\overline{f^2} - \tfrac{4}{3}\nu_2\overline{f^2}_\eta\big)u_{2\xi}$$
$$+ \big(2\sqrt{\tfrac{22}{5}}F_2 - \tfrac{18}{11}\overline{f^2} - \tfrac{1}{2}\nu_2\overline{f^2}_\eta\big)u_{2\xi\xi} + 2\nu_2 u_{2\xi\xi\xi} = 0, \quad \text{(B 4)}$$

where $f(\eta) = -(11/9)A(\eta)$.

Linear stability theory applied to equations (B 1) and (B 4) provides the corrections to the critical Froude number:

$$F_1 = -\frac{31}{968}\nu_1\sqrt{110}\overline{f}_\eta^2 + \frac{21\nu_1\sqrt{110}}{242}\overline{f_\eta\check{U}_{2\eta}} \qquad \text{(theory A)}, \quad \text{(B 5)}$$

$$F_2 = \frac{15\sqrt{110}}{968}\overline{f^2} + \frac{39\sqrt{110}}{968}\overline{f_\eta^2} \qquad \text{(theory B)}. \quad \text{(B 6)}$$

The correction for theory A can be written as

$$F_1 = \sum_{j=1}^{\infty}\left[\frac{315}{5324}\left(\frac{81}{121} + \nu_1^2 j^2\right)^{-1/2} - \frac{31}{968}\right]\frac{|A_j|^2}{\frac{81}{121} + \nu_1^2 j^2}, \quad \text{(B 7)}$$

where the expression in square brackets is positive for $j > 0$. Thus small-amplitude topography is stabilizing in both limits.

The amplitude equations (B 1) and (B 4) are similar to (5.23) and (5.25) although they cannot be conveniently factorized into the form (5.33). This failure can be traced to the fact that mass is advected at a different rate than momentum in the laminar model when the parameter $\alpha$ is not equal to unity. The change in the structure of the amplitude equation could conceivably affect the general character of the nonlinear roll-wave dynamics. However, we have not explored this in the current work.

REFERENCES

ALAVIAN, V. 1986 Behaviour of density currents on an incline. *J. Hydraulic Res.* **112**, 27–42.
ALEKSEENKO, S. V., NAKORYAKOV, V. E. & POKUSAEV, B. G. 1985 Wave formation on a vertical falling liquid film. *AIChE J.* **31**, 1446–1460.

BALMFORTH, N. J., IERLEY, G. R. & YOUNG, W. R. 2002 Tidal conversion by subcritical topography. *J. Phys. Oceanogr.* **32**, 2900–2914.

BENJAMIN, T. B. 1957 Wave formation in laminar flow down an inclined plane. *J. Fluid Mech.* **2**, 554–574.

BENNEY, D. J. 1966 Long waves on liquid films. *J. Maths and Phys.* **54**, 150–155.

BROCK, R. R. 1969 Development of roll-wave trains in open channels. *J. Hydraul. Div.* **95**, HY4, 1401–1427.

BROOK, B. S., PEDLEY, T. J. & FALLE, S. A. 1999 Numerical solutions for unsteady gravity-driven flows in collapsible tubes: evolution and roll-wave instability of a steady state. *J. Fluid Mech.* **396**, 223–256.

CABAL, A., SZUMBARSKI, J. & FLORYAN, J. M. 2002 Stability of flow in a wavy channel. *J. Fluid Mech.* **457**, 191–212.

CARVER, S., SEAR, D. & VALENTINE, E. 1994 An observation of roll waves in a supraglacial meltwater channel, Harlech Gletscher, East Greenland. *J. Glaciol.* **40**, 75–78.

CENEDESE, C., WHITEHEAD, J. A., ASCARELLI, T. A. & OHIWA, M. 2004 A dense current flowing down a sloping bottom in a rotating fluid. *J. Phys. Oceanogr.* **34**, 188–203.

CHANG, H.-C., DEMEKHIN, E. A. & KALAIDIN, E. 2000 Coherent structures, self-similarity and universal roll wave coarsening dynamics. *Phys. Fluids* **12**, 2268–2278.

CORNISH, V. 1910 *Ocean Waves and Kindred Geophysical Phenomena*. Cambridge University Press.

DRESSLER, R. F. 1949 Mathematical solution of the problem of roll waves in inclined channel flows. *Commun. Pure Appl. Maths* **2**, 149–194.

ENGELUND, F. & WAN, Z. 1984 Instablity of hyperconcentrated flow. *J. Hydraulic Res.* **110**, 219–233.

FER, I., LEMMIN, U. & THORPE, S. A. 2003 Winter cascading of cold water in lake geneva. *J. Geophys. Res.* **107** (C6), Art. no. 3060.

FLORYAN, J. M. 2002 Centrifugal instability of Couette flow over a wavy wall. *Phys. Fluids* **14**, 312–322.

FORTERRE, Y. & POULIQUEN, O. 2003 Long-surface-wave instability in dense granular flows. *J. Fluid Mech.* **486**, 21–50.

HWANG, S.-H. & CHANG, H.-C. 1987 Turbulent and inertial roll waves in inclined film flow. *Phys. Fluids* **30**, 1259–1268.

JEFFREYS, H. 1925 The flow of water in an inclined channel of rectangular bottom. *Phil. Mag.* **49**, 793.

JOSEPH, D. & RENARDY, Y. 1993 *Fundamentals of Two-Fluid Dynamics: Part 1, Mathematical Theory and Applications*. Springer.

JULIAN, B. R. 1994 Volcanic termor: Nonlinear excitation by fluid flow. *J. Geophys. Res.* **99**, 11859–877.

KAPITZA, P. L. & KAPITZA, S. P. 1949 Wave flow of thin viscous liquid films. *Zh. Exper. i Teor. Fiz.* **19**, 105–120.

KEVORKIAN, J., YU, J. & WANG, L. 1995 Weakly nonlinear waves for a class of linearly unstable hyperbolic conservation laws with source terms. *SIAM J. Appl. Maths* **55**, 446–484.

KOURIS, C. & TSAMOPOULOS, J. 2001 Core–annular flow in a periodically constricted circular tube. Part 1. Steady-state, linear stability and energy analysis. *J. Fluid Mech.* **432**, 31–28.

KRANENBURG, C. 1992 On the evolution of roll waves. *J. Fluid Mech.* **245**, 249–261.

MANDRE, S. 2001 Effect of bottom topography on roll wave instabilities. In *Proc. 2001 Geophysical Fluid Dynamics Summer Study Program*. Woods Hole Oceanographic Institution.

MONTES, S. 1998 *Hydraulics of Open Channel Flow*. ASCE Press.

NEEDHAM, D. J. & MERKIN, J. H. 1984 On roll waves down an open inclined channel. *Proc. R. Soc. Lond.* A **394**, 259–278.

PEDLEY, T. J. 1980 *Fluid Mechanics of Large Blood Vessels*. Cambridge University Press.

PROKOPIOU, T., CHENG, M. & CHANG, H.-C. 1991 Long waves on inclined films at high Reynolds number. *J. Fluid Mech.* **222**, 665–691.

PUMIR, A., MANNEVILLE, P. & POMEAU, Y. 1983 On solitary waves running down an inclined plane. *J. Fluid Mech.* **135**, 27–50.

ROUSE, H. 1938 *Fluid Mechanics for Hydraulic Engineers*. Dover.

SELVARAJAN, S., TULAPURKARA, E. G. & RAM, V. V. 1999 Stability characteristics of wavy walled channel flows. *Phys. Fluids* **11**, 579–589.

SHKADOV, V. Y. 1967 Wave conditions in flow of thin layer of a viscous liquid under the action of gravity. *Izv. Akad. Nauk SSSR, Mekh. Zhidh. Gaza* **1**, 43–50.

SWATERS, G. E. 2003 Baroclinic characteristics of frictionally destabilized abyssal overflows. *J. Fluid Mech.* **489**, 349–379.

VLACHOGIANNIS, M. & BONTOZOGLOU, V. 2002 Experiments on laminar film flow along a periodic wall. *J. Fluid Mech.* **457**, 133–156.

WEI, H.-H. & RUNSCHNITZKI, D. S. 2002 The weakly nonlinear interfacial stability of a core–annular flow in a corrugated tube. *J. Fluid Mech.* **466**, 149–177.

WOODS, B. D., HURLBURT, E. T. & HANRATTY, T. J. 2000 Mechanism of slug formation in downwardly inclined pipes. *Intl. J. Multiphase Flow* **26**, 977–998.

YIH, C.-S. 1963 Stability of liquid flow down an inclined plane. *Phys. Fluids* **6**, 321.

YU, J. & KEVORKIAN, J. 1992 Nonlinear evolution of small disturbances into roll waves in an inclined open channel. *J. Fluid Mech.* **243**, 575–594.

YU, J., KEVORKIAN, J. & HABERMAN, R. 2000 Weak nonlinear waves in channel flow with internal dissipation. *Stud. Appl. Maths* **105**, 143.